

# No evidence for small disk-like bulges in a sample of late-type spirals

L. Costantin<sup>1</sup>, J. Méndez-Abreu<sup>2</sup>, E. M. Corsini<sup>1,3</sup>, L. Morelli<sup>1,3</sup>, J. A. L. Aguerri<sup>4,5</sup>,  
E. Dalla Bontà<sup>1,3</sup>, and A. Pizzella<sup>1,3</sup>

<sup>1</sup> Dipartimento di Fisica e Astronomia “G. Galilei”, Università di Padova, vicolo dell’Osservatorio 3, 35122 Padova, Italy  
e-mail: [luca.costantin@studenti.unipd.it](mailto:luca.costantin@studenti.unipd.it)

<sup>2</sup> School of Physics and Astronomy, University of St. Andrews, SUPA, North Haugh, KY16 9SS St. Andrews, UK

<sup>3</sup> INAF – Osservatorio Astronomico di Padova, vicolo dell’Osservatorio 5, 35122 Padova, Italy

<sup>4</sup> Instituto de Astrofísica de Canarias, Calle Vía Láctea s/n, 38200 La Laguna, Tenerife, Spain

<sup>5</sup> Departamento de Astrofísica, Universidad de La Laguna, Calle Astrofísico Francisco Sánchez s/n, 38205 La Laguna, Tenerife, Spain

Received 21 December 2016 / Accepted 6 March 2017

## ABSTRACT

**Context.** About 20% of low-redshift galaxies are late-type spirals with a small or no bulge component. Although they are the simplest disk galaxies in terms of structure and dynamics, the role of the different physical processes driving their formation and evolution is not yet fully understood.

**Aims.** We investigated whether small bulges of late-type spirals follow the same scaling relations traced by ellipticals and large bulges and if small bulges are disk-like or classical bulges.

**Methods.** We derived the photometric and kinematic properties of nine nearby late-type spirals. To this aim, we analyzed the surface-brightness distribution from the *i*-band images of the Sloan Digital Sky Survey and obtained the structural parameters of the galaxies from a two-dimensional photometric decomposition. We found a bulge component in seven galaxies of the sample, while the remaining two resulted in pure disk galaxies. We measured the line-of-sight stellar velocity distribution within the bulge effective radius from the long-slit spectra taken with high spectral resolution at the Telescopio Nazionale *Galileo*. We used the photometric and kinematic properties of the sample bulges to study their location in the fundamental plane, Kormendy, and Faber-Jackson relations defined for ellipticals and large bulges.

**Results.** We found that our bulges satisfy some of the photometric and kinematic prescriptions for being considered disk-like bulges, such as small sizes and masses with nearly exponential light profiles, small bulge-to-total luminosity ratios, low stellar velocity dispersions, and ongoing star formation. However, each of these bulges follows the same scaling relations of ellipticals, massive bulges, and compact early-type galaxies so they cannot be classified as disk-like systems.

**Conclusions.** We find a single population of galaxy spheroids that follow the same scaling relations, where the mass seems to lead to a smooth transition in the photometric and kinematic properties from less massive bulges to more massive bulges and ellipticals.

**Key words.** galaxies: bulges – galaxies: formation – galaxies: fundamental parameters – galaxies: kinematics and dynamics – galaxies: photometry – galaxies: structure

## 1. Introduction

The question of whether the morphology of galaxies is mostly imprinted by the initial conditions of their formation or by the processes driving their evolution is still open. The *Hubble* scheme of morphological classification tells us that spirals range from early to late types mainly according to the bulge-to-disk luminosity ratio (see [Buta et al. 2015](#), for a review). Historically, this classification was performed by the visual inspection of galaxies on photographic plates. With the progress of imaging technology, new methods to quantify the prominence of the bulge component were developed. Nowadays, the description of spirals according to the bulge size is usually performed by applying a photometric decomposition (e.g., [Simard 1998](#); [Peng et al. 2002](#); [de Souza et al. 2004](#); [Méndez-Abreu et al. 2008a](#); [Erwin 2015](#)), which also provides a full description of the bulge light distribution. In this context, the bulge is photometrically defined as the extra component dominating the galaxy light above

the surface-brightness profile of the disk extrapolated in the inner regions of the galaxy. The bulge surface brightness is usually fitted with a Sérsic law spanning a large range of profile shapes, whereas the disk surface brightness is usually fitted with an exponential law ([Andredakis 1998](#); [Prieto et al. 2001](#); [Aguerri et al. 2005](#); [Méndez-Abreu et al. 2017b](#)).

The current paradigm separates bulges into two main categories, namely classical and disk-like bulges, according to their photometric, kinematic, and stellar population properties, which result from their different assembly histories ([Athanasoula 2005](#); [Fisher & Drory 2008](#); [Laurikainen & Salo 2016](#)).

In this picture, classical bulges are thought to be formed by rapid gravitational collapse of protogalactic gas clouds ([Eggen et al. 1962](#)) or by accretion during major ([Kauffmann 1996](#)) and minor merging events ([Aguerri et al. 2001](#); [Eliche-Moral et al. 2006](#)). Moreover, they could be formed as a consequence of primordial clump instabilities at high-*z* sinking rapidly toward the center on account of dynamical

friction (Noguchi 1999; Dekel et al. 2009; Bournaud 2016). Classical bulges are thought to be similar to low-luminosity ellipticals, as they are characterized by rounder shapes than their surrounding disks, power-law profiles, and old stellar populations (see Kormendy & Kennicutt 2004, for a review). Most of these bulges are consistent with isotropic oblate rotators (but see Méndez-Abreu et al. 2017a, for different findings) and follow the fundamental plane (FPR), Kormendy (KR), and Faber-Jackson (FJR) relations (Bender et al. 1992; Aguerri et al. 2005).

As their name suggests, disk-like bulges are reminiscent of disks. Their formation involves secular processes of redistribution of gas and stars driven by bars or environmental phenomena, including the accretion of low-density satellites (Eliche-Moral et al. 2011). They have ellipticities similar to those of their disks, nearly-exponential luminosity profiles, and young stellar populations (e.g., Fisher & Drory 2016). They are rotationally supported oblate spheroids (Méndez-Abreu et al. 2010) and tend to be low- $\sigma$  outliers in the FJR (Kormendy 2016).

More than 50% of edge-on galaxies, including our Milky Way, show a thick component swelling out of the disk plane, which has the shape of a box or a peanut, in their central parts (Lütticke et al. 2000a,b). Although these structures are usually called boxy/peanut (B/P) bulges, this terminology could be misleading because they are just part of edge-on bars and are related to their secular evolution (Combes & Sanders 1981; Chung & Bureau 2004). In fact, the fraction of barred galaxies is consistent with that of edge-on galaxies with B/P bulges (Eskridge et al. 2000). Moreover, numerical simulations of stellar orbits confirmed that B/P bulges are connected to bars (Bureau & Athanassoula 2005; Athanassoula 2013) and photometric and kinematic observations showed that B/P bulges share the same properties of bars (Méndez-Abreu et al. 2008b; Erwin & Debattista 2013). The whole picture is further complicated by the coexistence of classical and disk-like bulges in the same galaxy (Gadotti 2009; Kormendy & Barentine 2010; Erwin et al. 2015) and their combination with B/P structures in barred galaxies (de Lorenzo-Cáceres et al. 2012; Méndez-Abreu et al. 2014).

The population of late-type spirals comprises about 20% of the galaxies at low redshift (Nair & Abraham 2010) and is composed of disks with a small or no bulge component. Late-type spirals are characterized by the presence of large amounts of dust, ongoing star formation, and small-scale substructures both in the nucleus and along the arms (Carollo et al. 1997). Moreover, some of these spirals show a light excess and peculiar kinematics in the inner hundred parsecs due to the presence of a nuclear cluster (Böker et al. 2002; Seth et al. 2006), nuclear stellar disk (Morelli et al. 2010; Corsini et al. 2012), or nuclear bar (Erwin 2004; de Lorenzo-Cáceres et al. 2013). Thus, measuring and interpreting the properties of their bulges is particularly challenging. The extremely late-type spirals located at the end of the *Hubble* morphological sequence do not actually have a bulge component and are pure disk galaxies (Böker et al. 2002, 2003).

Although bulgeless spirals are the simplest disk galaxies in terms of structure and dynamics, the role of the different physical processes driving their formation and evolution is not yet fully understood. Indeed, hierarchical clustering scenarios are successful in explaining the assembly and growth of massive ellipticals, but do not fully account for the building of disk-dominated galaxies with little or no bulge (Kautsch et al. 2006). Despite the fact that Hopkins et al. (2009) showed that the gas content in mergers plays a significant role in the efficiency of

disk destruction and enables disks to survive, numerical simulations still have difficulty reproducing the observed fraction of extremely-late spirals in the local universe (Weinzirl et al. 2009; Kormendy et al. 2010; Zavala et al. 2012).

The proper way to classify galactic bulges would be distinguishing between their different formation scenarios, which led to different observed properties. Reconstructing the formation mechanism from observations is a hard task, but the way in which scaling relations are satisfied by galaxies reflects the general dynamical principles of how baryons settle into dark matter potential wells. Previous works reported some hints about differences between less and more massive bulges, suggesting different formation scenarios and/or evolution pathways (Graham & Guzmán 2003; Méndez-Abreu et al. 2008a). However, since observational studies on bulges were mostly focused on the prominent bulges, further efforts are required to explore the photometric and kinematic properties of small and low-mass bulges in nearby late-type spirals. In this paper, we aim to extend the scaling relations of bulges all the way down to the lowest mass regime studied so far.

The paper is organized as follows. We present the galaxy sample in Sect. 2. We explain the acquisition, reduction, and analysis of the photometric and spectroscopic data in Sects. 3 and 4, respectively. We investigate whether our small bulges follow the same scaling relations traced by ellipticals and large bulges in Sect. 5. We discuss the results and give our conclusions in Sects. 6 and 7, respectively. We adopt  $H_0 = 75 \text{ km s}^{-1} \text{ Mpc}^{-1}$ ,  $\Omega_M = 0.3$ , and  $\Omega_\Lambda = 0.7$  as cosmological parameters throughout this work.

## 2. Sample selection

We selected a volume-limited sample of 309 disk galaxies located within a radius of 100 Mpc and with  $M_r \leq -18$  mag using the Sloan Digital Sky Survey (SDSS) Data Release 6 (DR6) catalog (Adelman-McCarthy et al. 2008). Since small bulges are preferentially located in late-type spirals, we considered only galaxies with a light concentration index  $C = R_{90}/R_{50} < 2.5$ , where  $R_{50}$  and  $R_{90}$  are the radii enclosing 50% and 90% of the total galaxy luminosity, respectively. This corresponds to a Sérsic index  $n \leq 1.5$  (Conselice 2003; Graham et al. 2005). Since galaxies are randomly oriented, it is possible to derive their properties by taking into account only the objects within a inclination interval. Therefore, we restricted to low inclination galaxies with  $i < 45^\circ$  in order to perform a successful photometric decomposition. Finally, we chose the 30 closest objects to be representative of the low-inclined late-type galaxies, but we observed only 9 of these objects due to time and weather constraints during the spectroscopic observations.

The main properties of the sample galaxies are listed in Table 1, while the distributions of the  $r$ -band magnitudes of the volume-limited, representative, and final samples of galaxies are shown in Fig. 1. Our sample galaxies are all late-type spirals (Fig. 2), despite their morphological classification in Huertas-Company et al. (2011) and Makarov et al. (2014).

## 3. Surface photometry

### 3.1. Data reduction

We retrieved the flux-calibrated  $i$ -band images of the sample galaxies from the SDSS DR9 (Ahn et al. 2012). The choice of  $i$  band ensured us a sufficient spatial resolution ( $FWHM \approx 1$  arcsec) and depth (out to  $\mu_i \approx 25$  mag arcsec $^{-2}$ ), and minimized the

**Table 1.** Properties of the sample galaxies.

Galaxy	Coordinates	Type	$B_T$	$i$	$z$	$D$	Scale	$D_{25} \times d_{25}$	$M_{BT}^0$			
SDSS name	Alternative name	RA [h m s]	Dec [deg arcmin arcsec]	[mag]	[°]	[Mpc]	[pc arcsec <sup>-1</sup> ]	[arcsec]	[mag]			
(1)	(2)	(3)	(4)	(5)	(6)	(7)	(8)	(9)	(10)	(11)	(12)	(13)
SDSS J104054.43+143202.4	...	10 40 54.43	+14 32 02.4	...	Sa-Sb (0.48)	16.00	22.4	0.021	81.4	395	21 × 20	-19.0
SDSS J112139.74+112924.6	...	11 21 39.74	+11 29 24.6	...	Sc-Sd (0.47)	16.77	20.3	0.020	77.6	378	19 × 17	-18.1
SDSS J113642.30+545045.7	IC 2943	11 36 42.30	+54 50 45.7	Sa	Sc-Sd (0.49)	15.18	39.5	0.019	75.8	368	24 × 19	-19.6
SDSS J115243.42+014428.0	UGC 6854	11 52 43.42	+01 44 28.0	SBbc	Sa-Sb (0.49)	14.52	39.6	0.020	79.6	386	56 × 43	-20.2
SDSS J133253.11-011531.1	PGC 47684	13 32 53.11	-01 15 31.1	S?	Sa-Sb (0.35)	15.70	40.6	0.012	47.1	228	29 × 22	-18.3
SDSS J143227.42+272538.7	IC 4452	14 32 27.42	+27 25 38.7	Sa	Sc-Sd (0.62)	14.92	20.6	0.014	55.9	271	29 × 27	-19.2
SDSS J144425.40+415140.6	PGC 2188136	14 44 25.40	+41 51 40.6	...	S0 (0.36)	15.79	36.0	0.018	69.0	335	39 × 31	-18.6
SDSS J160324.17+205328.4	NGC 6035	16 03 24.17	+20 53 28.4	Sc	Sc-Sd (0.64)	14.20	29.0	0.016	62.2	301	59 × 52	-20.4
SDSS J170128.21+634128.0	IC 1241	17 01 28.21	+63 41 28.0	Sc	Sc-Sd (0.63)	14.37	38.2	0.016	63.4	308	70 × 56	-20.0

**Notes.** (1) Full name of the galaxy according to SDSS. (2) Alternative name. (3), (4) Right ascension and declination (J2000.0). (5) Morphological classification from HyperLeda (Makarov et al. 2014). (6) Morphological classification and corresponding probability from Huertas-Company et al. (2011). (7) Apparent total blue magnitude from HyperLeda. (8) Inclination from HyperLeda. (9) Spectroscopic redshift from SDSS DR6. (10) Angular diameter distance. (11) Conversion factor from arcsec to parsec. (12) Major and minor diameters of the isophote at a surface brightness level of  $\mu_B = 25$  mag arcsec<sup>-2</sup> from the HyperLeda. (13) Absolute total blue magnitude corrected for inclination and extinction from the HyperLeda.

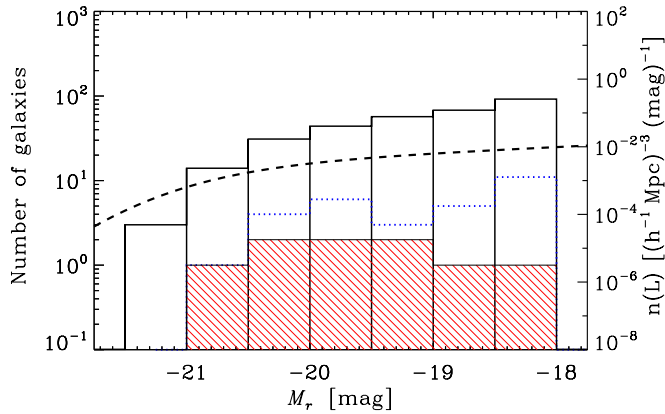


**Fig. 1.** Distribution of the absolute  $r$ -band magnitude of the volume-limited sample (309 galaxies, black solid line), representative sample of late-type spirals (30 galaxies, blue dotted line), and observed sample (9 galaxies, red filled histogram). The dashed line corresponds to the  $r$ -band luminosity function of SDSS galaxies by Tempel et al. (2011).

dust effects with respect to the other SDSS passbands to resolve the bulge component with an accurate photometric decomposition of the galaxy surface-brightness distribution.

The sky level provided by SDSS for each image consists of a global estimate across the field of view after masking the most luminous sources (Aihara et al. 2011). This proves to be unreliable in the analysis of the faintest outskirts of large galaxies like ours (Hyde & Bernardi 2009; Méndez-Abreu et al. 2017b). Therefore, we measured the sky level in the surroundings of each sample galaxy following the procedure proposed by Pohlen & Trujillo (2006) as applied in Corsini et al. (2017) and Morelli et al. (2016). We masked all the foreground stars, companion and background galaxies, and spurious sources, such as residual cosmic rays and bad pixels close to the galaxy, and measured its surface-brightness radial profile with the ellipse task in IRAF<sup>1</sup> (Jedrzejewski 1987). First, we allowed the center, ellipticity, and position angle of the fitting ellipses to vary. Then, we fitted again the isophotes with ellipse adopting the center of the inner ellipses and the ellipticity and position angle of

the outer ellipses. Finally, we assumed the constant value of the surface brightness measured at large radii, where the galaxy contributed no light, as the sky level to be subtracted from the image. We found that our estimates of the sky level are systematically lower by 0.2% than those given by SDSS. We measured the standard deviation  $\sigma_{\text{sky}}$  of the background in the sky-subtracted image by analyzing several regions where no sources were present with the IRAF task imexamine.

We trimmed the sky-subtracted images to reduce the computing time to perform a reliable photometric decomposition. Each galaxy was centered in a field of view of at least  $50 \times 50$  pixels corresponding to  $20 \times 20$  arcsec<sup>2</sup>. We ran ellipse on the trimmed images to derive the radial profiles of the ellipse-averaged surface brightness  $\mu$ , ellipticity  $\epsilon$ , and position angle PA of the galaxy isophotes in the  $i$  band. We adopted these photometric profiles and the mask images we built to estimate the sky level for the photometric decomposition.

We modeled the point spread function (PSF) with a circular Moffat profile (Moffat 1969; Trujillo et al. 2001), which is a reliable approximation for photometric decomposition of nearby galaxies in SDSS images (Méndez-Abreu et al. 2017b), and derived its parameters fitting five unsaturated stars with the IRAF task imexamine before trimming the image (Table 2).

### 3.2. Photometric decomposition

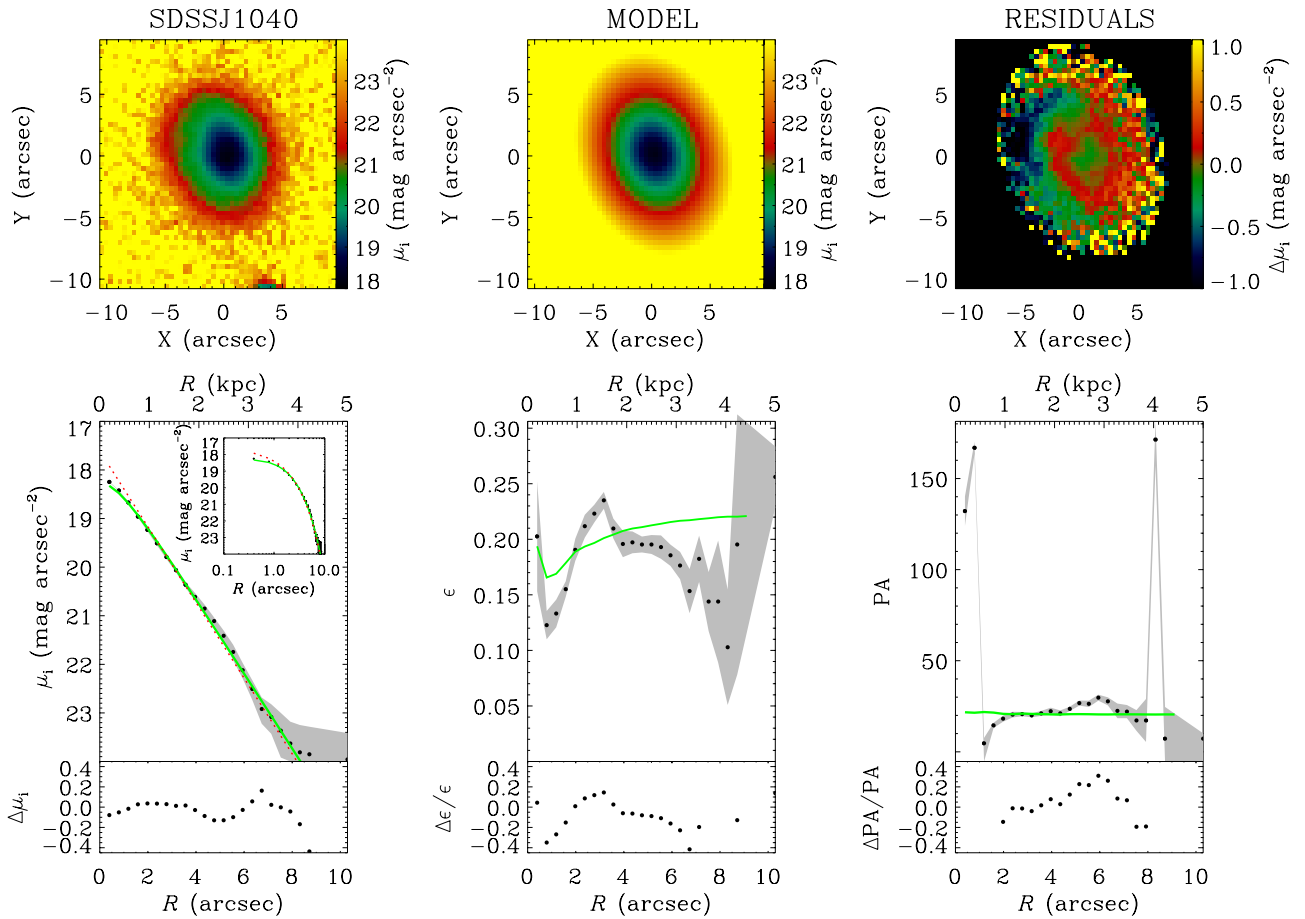
We derived the structural parameters of the sample galaxies by performing a two-dimensional photometric decomposition of their surface brightness distribution using the GASP2D algorithm (Galaxy Surface Photometry 2 Dimensional Decomposition) developed by Méndez-Abreu et al. (2008a, 2014) in IDL<sup>2</sup>. The GASP2D algorithm adopts a set of analytical functions to model the light contribution of the galaxy components. We assumed the surface brightness distribution of the sample galaxies to be the sum of a bulge, disk, and bar component. We did not consider any other additional component, such as spiral arms, lenses, or ovals. When possible, we masked their corresponding regions in the galaxy images and excluded them from the fitting process. In addition, we masked out the dust patches and lanes as much as possible to recover a reliable model of the surface-brightness distribution.

<sup>1</sup> Image Reduction and Analysis Facility is distributed by the National Optical Astronomy Observatory (NOAO), which is operated by the Association of Universities for Research in Astronomy (AURA), Inc. under cooperative agreement with the National Science Foundation.

<sup>2</sup> Interactive Data Language is distributed by ITT Visual Information Solutions. It is available from <http://www.itvis.com>

**Table 2.** Characteristics of the *i*-band SDSS images of the sample galaxies.

Galaxy	Gain	RON	Sky	<i>FWHM</i>	$\beta$
(1)	[ $e^- \text{ADU}^{-1}$ ]	[ $e^-$ ]	[ADU]	[arcsec]	(6)
SDSSJ1040	4.8	10.7	$212 \pm 6$	1.0	3.0
SDSSJ1121	6.6	16.4	$177 \pm 5$	1.1	3.4
SDSSJ1136	4.9	13.4	$230 \pm 6$	1.0	4.8
SDSSJ1152	6.6	16.4	$121 \pm 4$	1.0	2.7
SDSSJ1332	4.8	10.7	$184 \pm 5$	1.3	3.8
SDSSJ1432	6.6	16.4	$150 \pm 5$	1.0	5.6
SDSSJ1444	4.9	13.4	$199 \pm 5$	0.7	3.6
SDSSJ1603	6.6	16.4	$128 \pm 4$	0.9	4.7
SDSSJ1701	4.9	10.4	$119 \pm 5$	1.0	4.1

**Notes.** (1) Short name of the galaxy according to SDSS. (2) Image gain provided by SDSS. (3) Image readout noise provided by SDSS. (4) Measured sky level and corresponding standard deviation. (5), (6) *FWHM* and  $\beta$  parameter measured for the circular Moffat PSF.

**Fig. 2.** Two-dimensional photometric decomposition of the *i*-band images of the sample galaxies obtained from GASP2D. For each galaxy the *upper panels* (from left to right) show the map of the observed, modeled, and residual (observed–modeled) surface brightness distributions. The field of view is oriented with north up and east left. The *lower panels* (from left to right) show the ellipse-averaged radial profile of surface brightness, position angle, and ellipticity measured in the observed (black dots with gray error bars) and seeing-convolved modeled image (green solid line) and their corresponding difference. The intrinsic surface-brightness radial profiles of the best-fitting bulge (blue dashed line), disk (red dotted line), and bar component (magenta dot-dashed line) are also shown in both linear and logarithmic scale for the distance to the center of the galaxy. The complete version of this figure is available as Fig. B.1.

We used the Sérsic law (Sérsic 1968) to describe the surface brightness of the bulge component

$$I_{\text{bulge}}(x, y) = I_e 10^{-b_n \left[ \left( \frac{r_{\text{bulge}}}{r_e} \right)^{1/n} - 1 \right]}, \quad (1)$$

where  $r_e$  is the effective radius,  $I_e$  is the surface brightness at  $r_e$ ,  $n$  is a shape parameter describing the curvature of the surface brightness profile, and  $b_n = 0.868n - 0.142$  (Caon et al. 1993). We assumed the bulge isophotes to be elliptical and centered on the galaxy center  $(x_0, y_0)$  with constant position angle  $\text{PA}_{\text{bulge}}$

and constant axial ratio  $q_{\text{bulge}}$ . The radius  $r_{\text{bulge}}$  is given by

$$r_{\text{bulge}}(x, y) = \left[ \left( -(x - x_0) \sin \text{PA}_{\text{bulge}} + (y - y_0) \cos \text{PA}_{\text{bulge}} \right)^2 + \left( (x - x_0) \cos \text{PA}_{\text{bulge}} + (y - y_0) \sin \text{PA}_{\text{bulge}} \right)^2 / q_{\text{bulge}}^2 \right]^{1/2}. \quad (2)$$

We adopted the exponential law (Freeman 1970) to describe the surface brightness of the disk component

$$I_{\text{disk}}(x, y) = I_0 e^{-\left(\frac{r_{\text{disk}}}{h}\right)}, \quad (3)$$

where  $I_0$  is the central surface brightness and  $h$  is the scale length of the disk. We adopted elliptical isophotes for the disk, which were centered on the galaxy center  $(x_0, y_0)$  and had constant position angle  $\text{PA}_{\text{disk}}$  and constant axial ratio  $q_{\text{disk}}$ . The radius  $r_{\text{disk}}$  is given by

$$r_{\text{disk}}(x, y) = \left[ \left( -(x - x_0) \sin \text{PA}_{\text{disk}} + (y - y_0) \cos \text{PA}_{\text{disk}} \right)^2 + \left( (x - x_0) \cos \text{PA}_{\text{disk}} + (y - y_0) \sin \text{PA}_{\text{disk}} \right)^2 / q_{\text{disk}}^2 \right]^{1/2}. \quad (4)$$

The surface brightness of the bar was described using the projected surface density of a three-dimensional Ferrers ellipsoid (Ferrers 1877)

$$I_{\text{bar}}(x, y) = \begin{cases} I_{0,\text{bar}} \left[ 1 - \left( \frac{r_{\text{bar}}}{a_{\text{bar}}} \right)^2 \right]^{n_{\text{bar}}+0.5} & \text{if } r_{\text{bar}} \leq a_{\text{bar}} \\ 0 & \text{if } r_{\text{bar}} > a_{\text{bar}}, \end{cases} \quad (5)$$

where  $I_{0,\text{bar}}$  represents the central surface brightness,  $a_{\text{bar}}$  is the length, and  $n_{\text{bar}}$  is the shape parameter of the bar. We assumed that the isophotes of the bar were generalized ellipses (Athanasoula et al. 1990) centered on the galaxy center  $(x_0, y_0)$  with constant position angle  $\text{PA}_{\text{bar}}$  and constant axial ratio  $q_{\text{bar}}$ . The  $r_{\text{bar}}$  radius is defined as

$$r_{\text{bar}}(x, y) = \left[ \left| (y - y_0) \cos \text{PA}_{\text{bar}} - (x - x_0) \sin \text{PA}_{\text{bar}} \right|^c + \left| ((x - x_0) \cos \text{PA}_{\text{bar}} + (y - y_0) \sin \text{PA}_{\text{bar}}) / q_{\text{bar}} \right|^c \right]^{1/c}, \quad (6)$$

where  $c$  controls the shape of the bar isophotes. This serves the same purpose as the  $\cos 4\theta$  Fourier coefficient, which is usually adopted to describe the boxiness/diskyness of the isophotes (Jedrzejewski 1987; Bender & Moellenhoff 1987). A bar with pure elliptical isophotes has  $c = 2$ ; it is  $c > 2$  if the isophotes are boxy and  $c < 2$  if they are disky. Including the bar in the multi-component approach to the photometric decomposition is crucial to retrieve the correct bulge parameters. In fact, both the Sérsic index  $n$  and bulge-to-disk ratio  $B/T$  can be overestimated if the bar is not properly accounted for (Aguerri et al. 2005; Gadotti 2009; Méndez-Abreu et al. 2014).

We derived the best-fitting values of the structural parameters of the galaxy components by comparing the model of the surface brightness distribution  $I_{\text{mod}}$  with the observed photon counts of the galaxy  $I_{\text{obs}}$  in each image pixel  $(x, y)$  with a iterative procedure of nonlinear least-squares minimization based on a robust Levenberg-Marquardt method (Moré et al. 1980) using the IDL task MPFIT (Markwardt 2009). We convolved the model image with the circular Moffat PSF measured on the galaxy image to

deal with the seeing effects. Each image pixel was weighted according to the variance of its total observed photon counts due to the contribution of both the galaxy and sky, in which the photon noise limitation and readout noise of the detector were also taken into account.

We detected a bulge component in seven out of nine sample galaxies, whereas the remaining two (namely SDSSJ1040 and SDSSJ1121) were better fitted only with a disk component. We detected a bar component in four out of nine galaxies (namely SDSSJ1152, SDSSJ1444, SDSSJ1603, and SDSSJ1701). The best-fitting structural parameters of the sample galaxies are available in Table 3 while their GASP2D fits are shown in Fig. 2.

### 3.3. Error budget

The formal errors obtained from the  $\chi^2$  minimization procedure are usually not representative of the real errors in the structural parameters space (Méndez-Abreu et al. 2008a). Therefore, we estimated the errors by analyzing a sample of mock galaxies built through a series of Monte Carlo (MC) simulations to test the sensibility of the best-fitting parameters and understand if any systematic errors affect them.

Instead of randomly generating the mock galaxies, we created them taking into account the correlations among the structural parameters of bulge and disk. For this purpose we used the sample of nearby galaxies of Gadotti (2009). Firstly, we divided the 9 galaxies of our sample into three subsamples, according to the number of their components: (1) disk only; (2) bulge and disk; (3) bulge, disk, and bar. This allowed us to define bins of magnitude in which we created the corresponding sample of mock galaxies: four bins for subsamples (1) and (2) in the magnitude range  $-20.5 < M_i < -18.5$  mag and four bins for subsample (3) in the magnitude range  $-21.5 < M_i < -19.5$  mag. Each bin is composed of about 200 mock galaxies. Then, we generated a  $B/T$  random value from a uniform distribution in the range  $[0, 0.45]$ , and starting from this value we determined the Sérsic index  $n$  from a normal distribution using the correlation

$$n = 5.73 \cdot B/T + 1.25, \quad (7)$$

which we obtained by fitting the Gadotti (2009) sample. After that, we produced a random value of  $r_e$  from a normal distribution and determined a value of  $h$  using the correlation

$$r_e/h = 0.69 \cdot B/T + 0.19, \quad (8)$$

which we obtained from the sample of Gadotti (2009). Unfortunately, we could not use this sample to investigate the properties of the bar, so we randomly generated the structural parameters of the bar in the same intervals as those obtained from the photometric decomposition of our sample. The interval ranges explored for all the parameters were  $r_e = [0.5, 4]$  arcsec,  $n = [0.5, 4]$ ,  $h = [1, 14]$  arcsec,  $a_{\text{bar}} = [5, 25]$  arcsec,  $n_{\text{bar}} = [0, 7]$ , and  $c = [-2, 5]$ . Finally, we randomly generated the apparent flattening of the bulge  $q_{\text{bulge}}$ , disk  $q_{\text{disk}}$ , and bar  $q_{\text{bar}}$  and the values of the position angle of the bulge  $\text{PA}_{\text{bulge}}$ , disk  $\text{PA}_{\text{disk}}$ , and bar  $\text{PA}_{\text{bar}}$  from uniform distributions, where no constraints were adopted.

We assumed the mock galaxies to be at a distance of 69 Mpc, which corresponds to the median distance of our sample galaxies. We chose the pixel scale ( $0.396$  arcsec pixel $^{-1}$ ), gain ( $6.6 e^-$  ADU $^{-1}$ ), readout noise ( $16.4 e^-$  rms), and size of the simulated images ( $400 \times 400$  pixels) to mimic the instrumental setup of the photometric observations. Moreover, we added a background level ( $170$  ADU) and a Poissonian photon noise to

**Table 3.** Structural parameters of the sample galaxies.

Galaxy [name] (1)	$\mu_e$ [mag arcsec <sup>-2</sup> ] (2)	$\langle \mu_e \rangle$ [mag arcsec <sup>-2</sup> ] (3)	$r_e$ [arcsec] (4)	$n$ (5)	$e_b$ (6)	$\text{PA}_b$ [°] (7)	$\mu_0$ [mag arcsec <sup>-2</sup> ] (8)	$h$ [arcsec] (9)	$e_d$ (10)	$\text{PA}_d$ [°] (11)	$\mu_{\text{bar}}$ [mag arcsec <sup>-2</sup> ] (12)	$a_{\text{bar}}$ [arcsec] (13)	$n_{\text{bar}}$ (14)	$e_{\text{bar}}$ (15)	$\text{PA}_{\text{bar}}$ [°] (16)	$c$ (17)	$B/T$ (18)	$\text{Bar}/T$ (19)
SDSSJ1040	...	...	...	...	...	...	17.611 ± 0.005	1.394 ± 0.008	0.238 ± 0.004	20.4 ± 0.5	...	...	...	...	...	...	0	0
SDSSJ1121	...	...	...	...	...	...	18.299 ± 0.005	1.312 ± 0.007	0.050 ± 0.004	19.0 ± 0.5	...	...	...	...	...	...	0	0
SDSSJ1136	19.0 ± 0.1	18.3 ± 0.1	1.3 ± 0.1	1.06 ± 0.07	0.15 ± 0.02	172 ± 2	18.74 ± 0.04	3.17 ± 0.05	0.10 ± 0.01	128 ± 2	...	...	...	...	...	...	0.20	0
SDSSJ1152	20.1 ± 0.2	19.0 ± 0.5	2.9 ± 0.4	2.3 ± 0.2	0.75 ± 0.01	7 ± 2	20.77 ± 0.08	11.1 ± 0.3	0.23 ± 0.02	80 ± 2	20.87 ± 0.09	15 ± 2	6 ± 3	0.77 ± 0.02	32.6 ± 0.3	0.43 ± 0.06	0.10	0.03
SDSSJ1332	20.2 ± 0.1	19.3 ± 0.2	1.3 ± 0.1	1.6 ± 0.1	0.050 ± 0.02	56 ± 2	19.12 ± 0.04	3.30 ± 0.06	0.038 ± 0.01	60 ± 2	...	...	...	...	...	...	0.12	0
SDSSJ1432	19.2 ± 0.1	18.6 ± 0.1	0.85 ± 0.07	0.94 ± 0.06	0.38 ± 0.02	3 ± 2	18.53 ± 0.04	3.49 ± 0.06	0.080 ± 0.01	90 ± 2	...	...	...	...	...	...	0.04	0
SDSSJ1444	18.7 ± 0.2	17.5 ± 0.5	0.63 ± 0.09	2.7 ± 0.3	0.15 ± 0.01	122 ± 2	20.18 ± 0.08	5.9 ± 0.1	0.21 ± 0.02	180 ± 2	21.22 ± 0.09	12 ± 2	2.0 ± 0.8	0.73 ± 0.02	159.3 ± 0.3	0.01 ± 0.01	0.12	0.06
SDSSJ1603	19.2 ± 0.2	18.5 ± 0.2	0.92 ± 0.09	0.99 ± 0.07	0.186 ± 0.009	126 ± 1	19.82 ± 0.08	9.9 ± 0.2	0.061 ± 0.01	160 ± 1	21.99 ± 0.08	6 ± 1	0.11 ± 0.04	0.72 ± 0.01	102.0 ± 0.2	2.0 ± 0.2	0.03	0.01
SDSSJ1701	17.5 ± 0.2	16.7 ± 0.4	0.54 ± 0.05	1.23 ± 0.09	0.217 ± 0.009	39 ± 1	19.87 ± 0.08	8.9 ± 0.2	0.11 ± 0.01	60 ± 1	21.03 ± 0.08	17 ± 3	2.0 ± 0.8	0.75 ± 0.01	69.3 ± 0.2	-1.0 ± 0.1	0.06	0.03

**Notes.** (1) Short name of the galaxy according to SDSS. (2), (3), (4), (5), (6) and (7) Surface brightness at effective radius, mean surface brightness within effective radius, effective radius, Sérsic index, ellipticity ( $e_{\text{bulge}} = 1 - q_{\text{bulge}}$ ), and position angle of the bulge, respectively. (8), (9), (10) and (11) Central surface brightness, scalelength, ellipticity ( $e_{\text{disk}} = 1 - q_{\text{disk}}$ ), and position angle of the disk, respectively. (12), (13), (14), (15), (16) and (17) Central surface brightness, length, Sérsic index, ellipticity ( $e_{\text{bar}} = 1 - q_{\text{bar}}$ ), position angle, and isophotal shape parameter of the bar, respectively. (18) Bulge-to-total luminosity ratio. (19) Bar-to-total luminosity ratio.

yield, in the simulated images, signal-to-noise ratios (S/N) similar to those of the observed images.

We analyzed the images of the mock galaxies as if they were real using GASP2D. Thus, we evaluated the initial conditions in the fitting procedure starting from the values of the generated parameters for each model galaxy. We estimated the errors on the fitted parameters by comparing the input and measured values, assuming they were normally distributed. For  $I_e$ ,  $r_e$ ,  $n$ ,  $I_0$ ,  $h$ ,  $I_{0,\text{bar}}$ ,  $a_{\text{bar}}$ ,  $n_{\text{bar}}$ , and  $c$  we adopted the mean and standard deviation of the relative errors of the mock galaxies as the systematic and statistical errors of the observed galaxies, respectively. For  $q_{\text{bulge}}$ ,  $q_{\text{disk}}$ ,  $q_{\text{bar}}$ ,  $\text{PA}_{\text{bulge}}$ ,  $\text{PA}_{\text{disk}}$ , and  $\text{PA}_{\text{bar}}$  we adopted the mean and standard deviation of the absolute errors of the mock galaxies as the systematic and statistical errors of the observed galaxies, respectively. The computed errors  $\sigma^2 = \sigma_{\text{stat}}^2 + \sigma_{\text{syst}}^2$  are provided in Table 3 because the systematic errors  $\sigma_{\text{syst}}$  are negligible compared to the statistical errors  $\sigma_{\text{stat}}$ . In the analysis we did not consider the systematic errors derived from the uncertainties on the estimates of the PSF FWHM or sky level. Therefore, the errors reported in Table 3 could be slightly underestimated (see Méndez-Abreu et al. 2008a, for a discussion).

Finally, we investigated the accuracy in measuring the structural parameters of the bulges of the sample galaxies in spite of their small size and demonstrated that we obtained reliable values (Appendix A).

## 4. Long-slit spectroscopy

### 4.1. Observations and data reduction

We carried out the spectroscopic observations of the sample galaxies on 2009 April 1–4 at the Telescopio Nazionale Galileo (TNG) in La Palma (Spain).

In the setup we used the DOLORES spectrograph with the V510 grism covering the wavelength range 4875–5325 Å and the 1-arcsec wide slit. The spectrograph was equipped with a E2V 4240 camera and a thinned back-illuminated, deep-depleted, Astro-BB coated CCD with 2048 × 2048 pixels of 13.5 × 13.5 μm<sup>2</sup>, gain 0.97 e<sup>-</sup> ADU<sup>-1</sup>, and readout noise 9 e<sup>-</sup> (rms). We used the mean of the Gaussian FWHMs measured for a number of unblended arc-lamp lines over the whole spectra range of a wavelength-calibrated spectrum to derive the instrumental resolution. We found  $FWHM_{\text{inst}} = 1.04 \pm 0.08$  Å, corresponding to a velocity dispersion  $\sigma_{\text{inst}} = 25.4 \pm 0.4$  km s<sup>-1</sup> at 5100 Å, far below the instrumental resolution of the SDSS spectra. The angular sampling was 0.252 arcsec pixel<sup>-1</sup> with a reciprocal dispersion of 0.235 Å pixel<sup>-1</sup>. The median value of the seeing FWHM during the observing nights was 1.22 arcsec. This value was measured fitting a circular Gaussian on the guide stars.

For each object, we centered the slit on the galaxy nucleus and visually aligned it along the galaxy major axis. Details about the slit position angles and exposure times are given in Table 4.

Each spectrum was bias-subtracted, flat-field corrected, cleaned of cosmic rays, corrected for bad columns, and wavelength and flux calibrated via standard IRAF tasks. We used the bias frames obtained during the observing nights to determine the bias level. We performed the flat-field correction for pixel-to-pixel sensitivity variations and large-scale illumination patterns arising from slit vignetting with thorium lamp and twilight sky spectra, respectively, which were normalized and divided into all spectra. We carried out the identification of the cosmic rays by comparing the counts in each pixel with the local mean and

**Table 4.** Log of spectroscopic observations and stellar kinematics of the sample galaxies.

Galaxy	PA	Single Exp. Time	Total Exp. Time	$\sigma_e$	$\sigma_{1.5 \text{ arcsec}}$
(1)	[ $^\circ$ ]	[s]	[h]	[ $\text{km s}^{-1}$ ]	[ $\text{km s}^{-1}$ ]
SDSSJ1040	16.9	$1 \times 1800 + 2 \times 2700$	2	...	$54 \pm 4$
SDSSJ1121	53.2	$1 \times 1800 + 2 \times 2700$	2	...	$37 \pm 4$
SDSSJ1136	24.9	$4 \times 1800$	2	$61 \pm 3$	$61 \pm 3$
SDSSJ1152	99.2	$4 \times 1800$	2	$55 \pm 11$	$58 \pm 11$
SDSSJ1332	88.4	$4 \times 1800$	2	$35 \pm 2$	$35 \pm 2$
SDSSJ1432	101.8	$1 \times 2400 + 1 \times 2700$	1.4	$37 \pm 4$	$42 \pm 3$
SDSSJ1444	-115.0	$3 \times 1800 + 1 \times 2700$	2.25	$55 \pm 9$	$68 \pm 7$
SDSSJ1603	9.8	$4 \times 1800$	2	$57 \pm 5$	$56 \pm 4$
SDSSJ1701	-24.0	$4 \times 1800$	2	$71 \pm 7$	$69 \pm 6$

**Notes.** (1) Short name of the galaxy according to SDSS. (2) Position angle of the slit measured north to east. (3) Exposure time of the spectra. (4) Total exposure time. (5) Measured velocity dispersion within  $r_e$ . (6) Measured velocity dispersion within 1.5 arcsec.

standard deviation as obtained from Poisson statistics considering the gain and readout noise of the CCD and then we corrected by interpolating over. If residual cosmic rays were present, we manually removed them by editing the spectra. We rebinned all the spectra using the wavelength solution obtained from the corresponding arc-lamp spectrum and flux-calibrated using the sensitivity function acquired from the flux standard star spectra of the corresponding night. We estimated the contribution from the sky by interpolating along the outermost regions at the two edges of the slit, where the galaxy or stellar light is negligible, and then we subtracted it. Finally, in order to improve the S/N of the final two-dimensional spectrum, we coadded the major-axis spectra using the center of the stellar continuum as reference.

#### 4.2. Stellar kinematics

We measured the stellar kinematics of the sample galaxies from the absorption features in their spectra. We used the penalized pixel-fitting method (pPXF; Cappellari & Emsellem 2004), including the Gas and Absorption Line Fitting algorithm (GANDALF; Sarzi et al. 2006), adapted for dealing with our setup. We rebinned the spectra along the spatial direction to provide the kinematic parameters within 1.5 arcsec and  $r_e$ .

The convolution of a linear combination of stellar spectra from the ELODIE library ( $FWHM = 0.48 \text{ \AA}$ ; Prugniel & Soubiran 2001) with the line-of-sight velocity distribution (LOSVD), described by Gauss-Hermite expansion (Gerhard 1993; van der Marel & Franx 1993), allowed us to fit the observed galaxy spectrum by  $\chi^2$  minimization in pixel space. Before the convolution, we degraded the spectral resolution of the ELODIE spectra by convolving them with a Gaussian function to match the galaxies spectral resolution. We properly masked bad pixels coming from imperfect subtraction of cosmic rays and sky emission lines and we excluded them from fitting procedure. In this way, we determined the value of the mean velocity  $v_{\text{los}}$ , velocity dispersion  $\sigma_{\text{los}}$ , and third-  $h_3$  and fourth-order  $h_4$  moments of the LOSVD. The measured values of  $h_3$  and  $h_4$  were compatible with zero, thus we fixed their values and we again performed the fit adopting a Gaussian LOSVD and obtaining only  $v_{\text{los}}$  and  $\sigma_{\text{los}}$ . All the analyzed spectra had a  $S/N \geq 20$  per resolution element (Fig. 3). We adopted a low-order multiplicative polynomial in the template fitting to deal with the effect of dust and possible residuals of the data reduction procedure. Thus, the method minimizes the effects of reddening because

it is more sensitive to the absorption lines than the continuum shape.

To allow for additional structure that is not addressed by our model, we estimated the uncertainties in the kinematic parameters from the formal errors of the fitting procedure by evaluating the  $\chi^2$  values. We achieved  $\chi^2 = N_{\text{dof}} = N_{\text{data}} - N_{\text{fit}}$  for the best-fitting model, where  $N_{\text{dof}}$ ,  $N_{\text{data}}$ , and  $N_{\text{fit}}$  are the numbers of the degrees of freedom, data points, and fitting parameters, respectively (Press et al. 1992). The measured stellar velocity dispersions and corresponding errors are reported in Table 4.

#### 5. Scaling relations

The luminosity, surface brightness, size, and velocity dispersion of ellipticals and bulges of disk galaxies are used to identify a set of well-defined scaling relations, namely the FPR, KR, and FJR. These relations unveil the structure of galaxy spheroids and provide valuable clues regarding the physics driving their formation and evolution history.

We investigated whether small bulges follow the same scaling relations traced by ellipticals and large bulges by comparing our galaxy sample to the sample of nearby galaxies, in which structural parameters and velocity dispersion are measured by Gadotti (2009) and Oh et al. (2011) from SDSS  $i$ -band images and spectra, respectively.

We marked all the comparison galaxies by assigning a probability to be E-S0, Sa-Sb, or Sc-Sd using the Bayesian automated classification by Huertas-Company et al. (2011). After that, ellipticals ( $B/T = 1$ ) were disentangled from lenticulars ( $B/T < 1$ ). This allowed us to properly consider the structural parameters of the whole galaxy for ellipticals and of the bulge component only for disk galaxies.

We are particularly interested in having low- $\sigma$  galaxies in the comparison sample. But, given the typical S/N and instrumental resolution of the SDSS spectra ( $\sigma_{\text{inst,SDSS}} \simeq 70 \text{ km s}^{-1}$ ), as a rule the use of SDSS galaxies with  $\sigma < 70 \text{ km s}^{-1}$  is not recommended because their velocity dispersion could be unreliable (Bernardi et al. 2003a). Oh et al. (2011) defined a new criterion to assess the reliability of the SDSS-based  $\sigma$  values by rejecting galaxies with a ratio  $rN/sN > 3$  between the rms of the residuals of the spectral fit ( $rN$ ) and the expected statistical rms ( $sN$ ). We eventually included in the comparison sample all the galaxies with  $\sigma < 70 \text{ km s}^{-1}$  that meet the prescription by Oh et al. (2011).

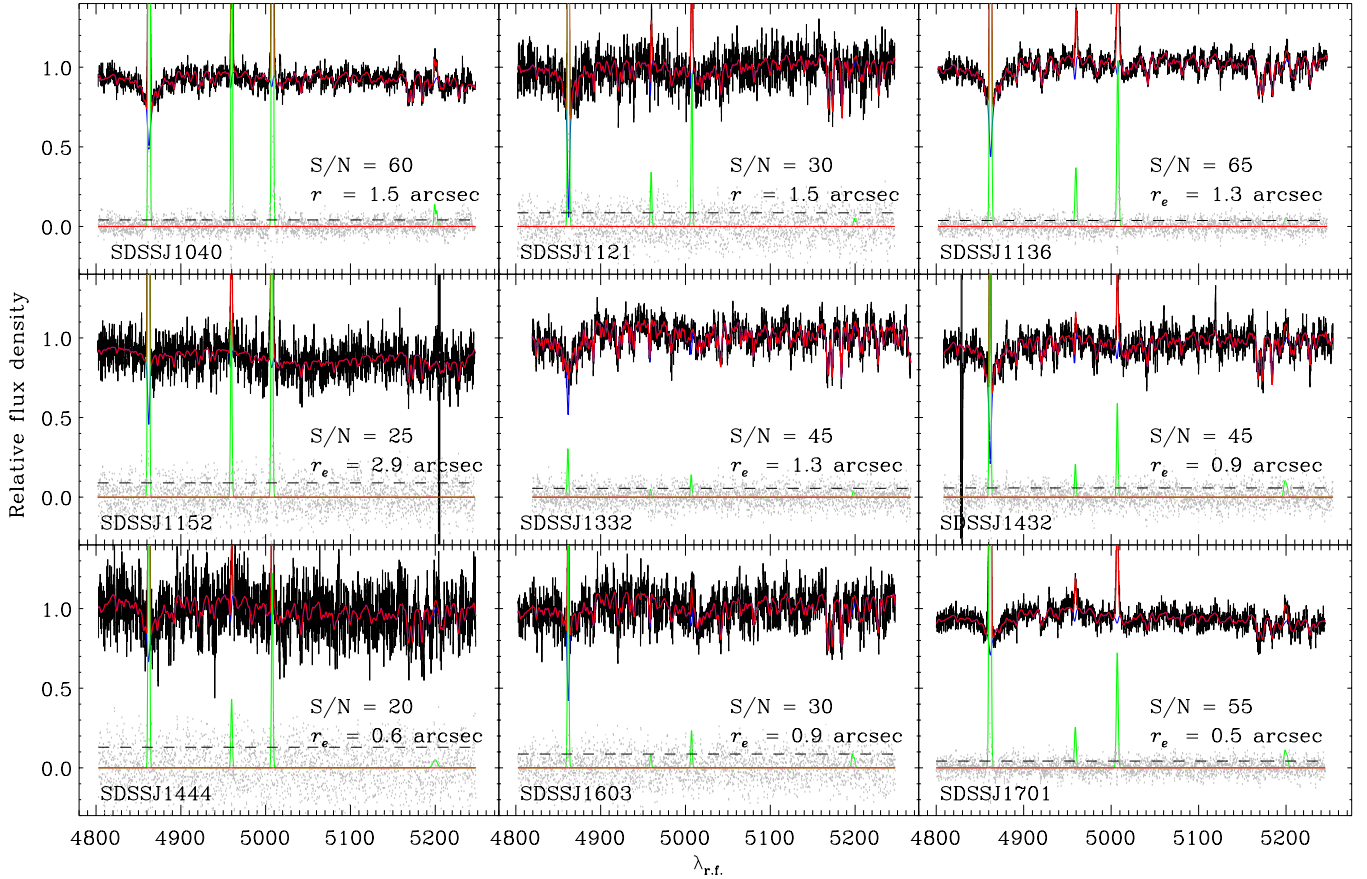


**Fig. 3.** Spectra of the sample galaxies. Relative fluxes have false zero points for viewing convenience. In each panel the best-fitting model (red line) is the sum of the spectra of the ionized gas (green line) and stellar component (blue line). The residuals (gray dots) are obtained by subtracting the best-fitting model from the observed spectrum. The S/N is given per resolution element.

For all the comparison galaxies we calculated the velocity dispersion  $\sigma_e$  within  $r_e$  from the SSDS  $\sigma$  measured within a fixed aperture of 3 arcsec using a power-law function

$$\left(\frac{\sigma}{\sigma_e}\right) = \left(\frac{r}{r_e}\right)^\alpha, \quad (9)$$

where  $\alpha$  is

$$\alpha_{\text{ETG}} = -0.055 \pm 0.020$$

for the early-type galaxies (ETGs), and

$$\begin{cases} \alpha_{\text{LTG}}(M_r < -22) = 0.047 \pm 0.021 \\ \alpha_{\text{LTG}}(-20 < M_r < -22) = 0.086 \pm 0.013, \\ \alpha_{\text{LTG}}(M_r > -20) = 0.153 \pm 0.063 \end{cases}$$

for the late-type galaxies (LTGs), as derived by Falc3n-Barroso et al. (2017) from the analysis of 300 galaxies drawn from the Calar Alto Legacy Integral Field Area Survey (CALIFA) DR3 (S3nchez et al. 2016).

Finally, the comparison sample includes 234 ellipticals and 626 bulges (79 in lenticulars, 192 in Sa-Sb galaxies, and 355 in Sc-Sd galaxies). For the sake of completeness, although only 7 out of 9 galaxies in our sample present a bulge component, the entire sample was superimposed on the scaling relations for a comparison. Owing to the small size of our sample, in the following we only discuss the properties of our individual late-type bulges and not of the whole population. Further observations of a complete sample of late-type bulges would be needed to infer their global properties as a distinct class of bulges.

### 5.1. Fundamental plane

The FPR (Djorgovski & Davis 1987; Dressler et al. 1987; D’Onofrio et al. 2008; Cappellari et al. 2013) is the most widely studied scaling relation providing information about structure and kinematics of galaxy spheroids. Observable quantities, such as the mean effective surface brightness  $\langle\mu_e\rangle$ ,  $r_e$ , and  $\sigma$  are commonly adopted in the FPR as proxies of the physical properties of the galaxy (Bender et al. 1992). When spirals are considered, as in this work, the previous properties only refer to the bulge component instead of the whole galaxy as in ellipticals.

The common way to express the FPR is  $\log(r_e) = \alpha \log(\sigma_e) + \beta\langle\mu_e\rangle + \gamma$  in order to separate  $r_e$  from  $\sigma_e$  and  $\langle\mu_e\rangle$ , which do not depend on distance. Figure 4 shows the FPR for the comparison sample of ellipticals and bulges with the best-fitting line given by

$$\log(r_e) = 0.99 \log(\sigma_e) + 0.24\langle\mu_e\rangle - 6.46, \quad (10)$$

where  $r_e$  is given in kpc,  $\sigma_e$  in  $\text{km s}^{-1}$ , and  $\langle\mu_e\rangle$  in  $\text{mag arcsec}^{-2}$ . We derived the FPR coefficients with a direct fit approach using the cramer routine in IDL. They are consistent with those found by Bernardi et al. (2003b) considering a sample of 8022 ETGs and analyzing their *i*-band images from the SDSS. The rms deviation in  $\log(r_e)$  from the fitted relation ( $\text{rms} = 0.15$ ) is larger than that obtained by Bernardi et al. (2003b), but similar to the *K*-band and *B*-band values of Falc3n-Barroso et al. (2002) and to the *V*-band value of Falc3n-Barroso et al. (2011), respectively. In the literature there is a general agreement that the typical scatter of the FPR ( $\text{rms} \simeq 0.10$ ) is independent of the

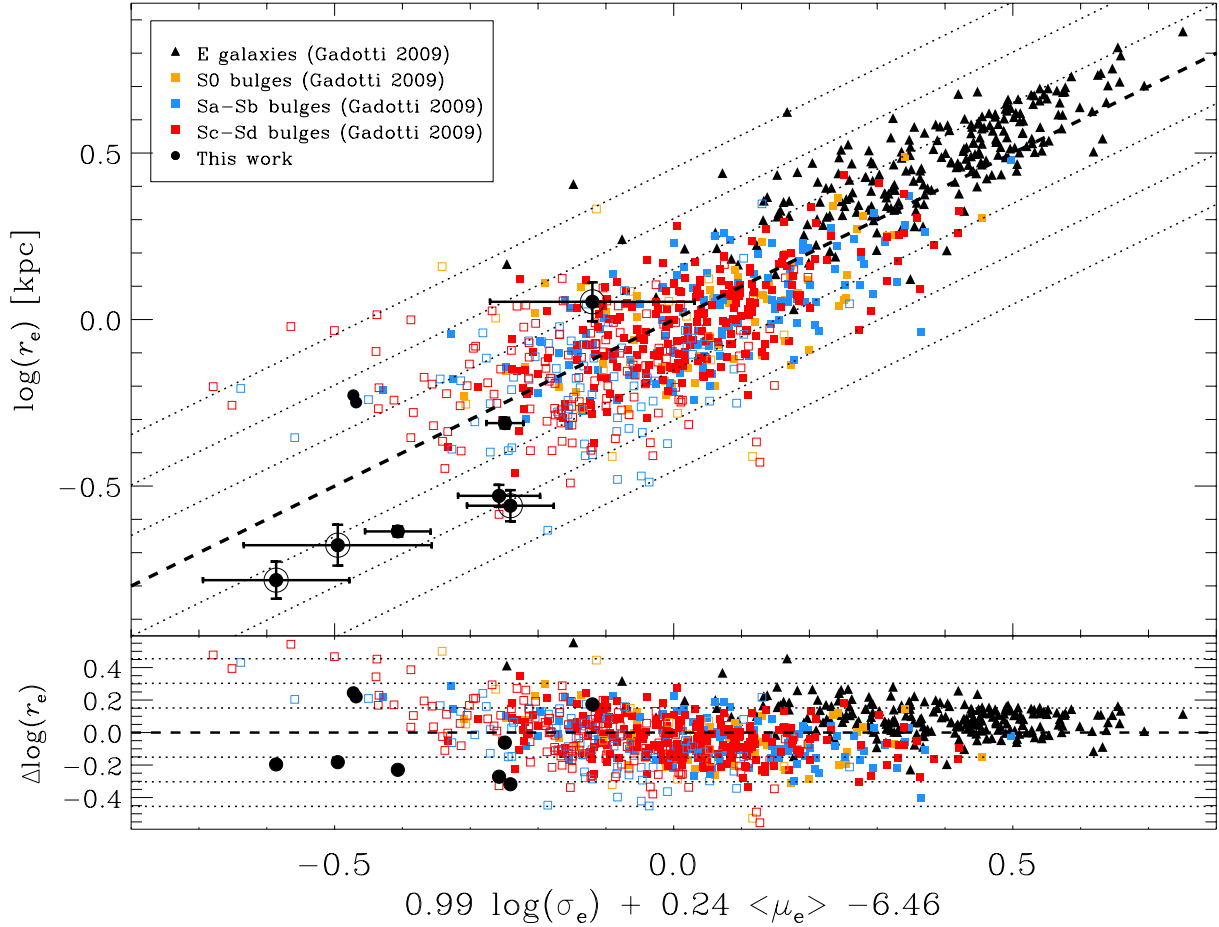


**Fig. 4.** Fundamental plane relation for the galaxies of our (larger symbols) and comparison sample (smaller symbols). The ellipticals (black triangles) and bulges in S0 (orange squares), Sa-Sb (blue squares), and Sc-Sd galaxies (red squares) of the comparison sample are shown with filled ( $\sigma > 70 \text{ km s}^{-1}$ ) and empty symbols ( $\sigma < 70 \text{ km s}^{-1}$ ) according to their calculated velocity dispersion. Filled circles with and without error bars correspond to the galaxies in our sample with and without bulge, respectively. Open circles denote the barred galaxies. The dashed line is the best-fitting relation for the comparison sample. The dotted lines show the 1 rms, 2 rms, and 3 rms deviation in  $\log(r_e)$  regions, respectively.

photometric passband (Jorgensen et al. 1996; La Barbera et al. 2010; Kim et al. 2016). But most works concentrate on ellipticals and lenticulars and adopt different fitting methods.

As a matter of fact, it is observationally easier to study the large and bright bulges of lenticulars and early-type spirals than the small and faint bulges of late-type spirals, which are more affected by dust patches and lanes and require more complex photometric decompositions (Laurikainen et al. 2010). Since they share similar properties, it is considered that ellipticals and early-type bulges usually follow the same FPR in optical and near-infrared passbands, whereas late-type bulges deviate from the relation (Falcón-Barroso et al. 2002). Some authors explained the deviation of late-type bulges from the FPR by taking into account the total kinetic energy of the system (Bender et al. 1992; Falcón-Barroso et al. 2002). Correcting the velocity dispersion for this missing contribution allows the placement of bulges of different morphological types on the same FPR (Bender et al. 1992; Falcón-Barroso et al. 2002). We measured the rotational velocity of our sample bulges within  $r_e$ . After correcting for slit orientation and galaxy inclination, we found that the maximum rotational velocity  $v_{\text{max}}$  is much smaller than the corresponding  $\sigma_e$ , which is  $v_{\text{max}} \simeq 50 \text{ km s}^{-1}$  for SDSSJ1152 and  $|v_{\text{max}}| < 30 \text{ km s}^{-1}$  for the remaining galaxies. The slit misalignment does not affect  $\sigma_e$  which we measured over nearly squared apertures. Thus, the correction of the velocity dispersion values

does not affect the position of the bulges in the FPR, although these measurements are subject to our observational limits in terms of both the large PSF FWHM of our spectra with respect to  $r_e$  and possible contamination from the underlying disk. However, the surface-brightness distribution is dominated by the bulge contribution by a factor 2–10 with respect to the disk inside  $r_e$ . Therefore, we are confident that our luminosity-weighted spectroscopic measurements are probing the bulge kinematics.

Each of our bulges is consistent with the FPR of the comparison sample (Fig. 4). No obvious differences appear in the residuals when galaxies are divided according to their morphological type. Moreover, the FPR suggests that a single population of bulges share the same physical properties. This is also true when our small bulges are considered.

## 5.2. Kormendy relation

According to the KR (Kormendy 1985; Nigoche-Netro et al. 2008) larger galaxies are fainter than smaller galaxies. Figure 5 shows the KR for the comparison sample of ellipticals and bulges with the best-fitting line given by

$$\langle \mu_e \rangle = 0.77(\pm 0.08) \log(r_e) + 18.84(\pm 0.02), \quad (11)$$

where  $\langle \mu_e \rangle$  is expressed in  $\text{mag arcsec}^{-2}$  and  $r_e$  in kpc. We derived the KR coefficients using the `poly_fit` routine in IDL.

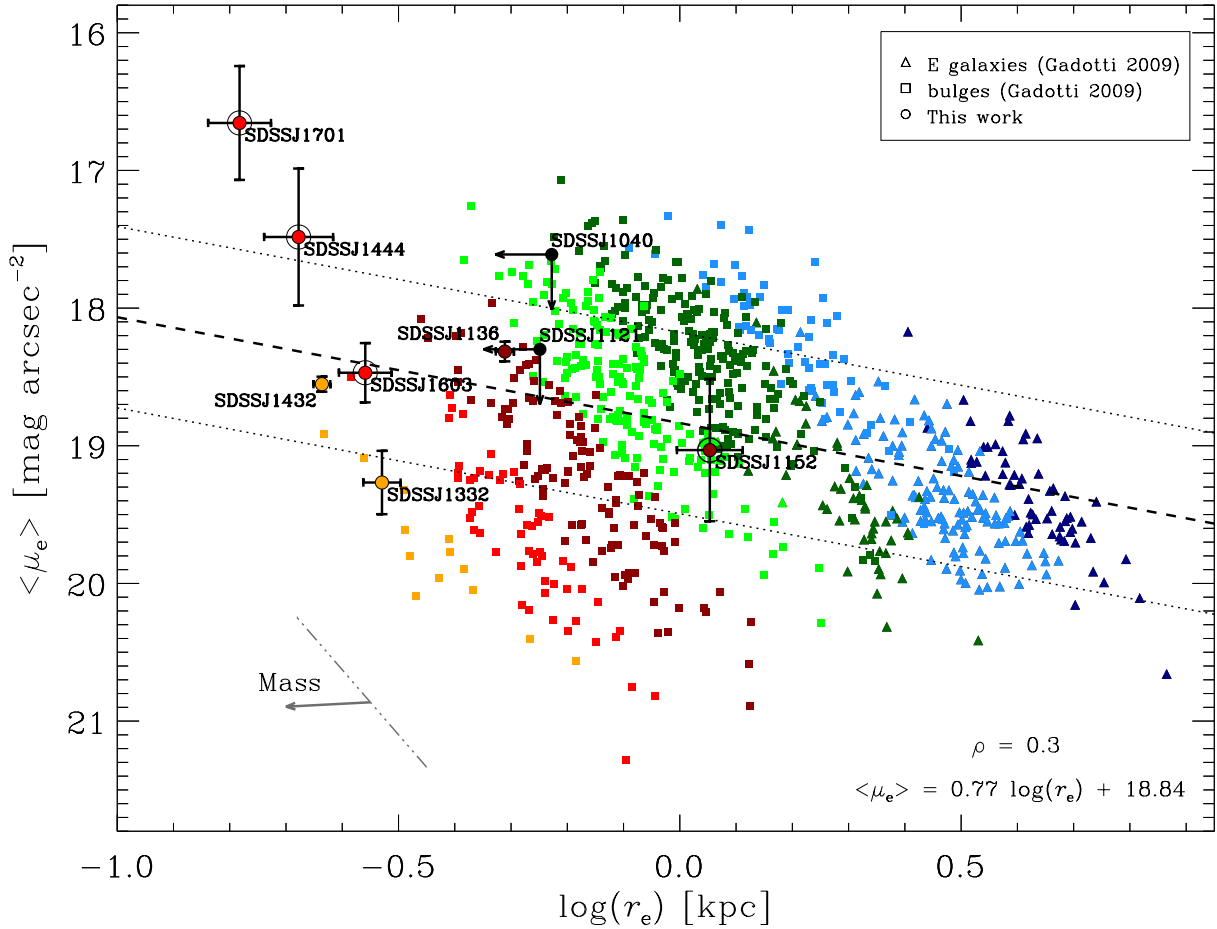


**Fig. 5.** Kormendy relation for the galaxies of our (larger symbols) and comparison sample (smaller symbols). The ellipticals and bulges of the comparison sample are shown with triangles and squares, respectively. Filled circles with and without error bars correspond to the galaxies in our sample with and without bulge, respectively. Open circles indicate the barred galaxies. The galaxies are divided according to their absolute magnitude in the following bins:  $M_i < -22$  mag (dark blue),  $M_i = [-22, -21]$  mag (light blue),  $M_i = [-21, -20]$  mag (dark green),  $M_i = [-20, -19]$  mag (light green),  $M_i = [-19, -18]$  mag (dark red),  $M_i = [-18, -17]$  mag (light red), and  $M_i = [-17, -16]$  mag (orange). The dashed line is the best-fitting relation for the comparison sample. The dotted lines show the rms deviation in  $\langle \mu_e \rangle$  from the fit. The dash-dotted line gives the slope of the KR for the magnitude bin  $M_i = [-20, -19]$  mag, while the arrow indicates the KR trend for decreasing masses (Nigoche-Netro et al. 2008). The best-fitting relation and Pearson correlation coefficient are also given.

The low value of the Pearson correlation coefficient ( $\rho = 0.3$ ) reflects the large scatter of the relation when all the comparison galaxies are considered together. The rms deviation in  $\langle \mu_e \rangle$  from the fitted relation (rms = 0.7 mag arcsec<sup>-2</sup>) is slightly larger than values quoted in earlier works (e.g., Hamabe & Kormendy 1987; La Barbera et al. 2003) making it difficult to observe a clear trend, contrary to previous findings (e.g., Aguerrí et al. 2004; Ravikumar et al. 2006). However, comparing galaxies with different absolute magnitudes could be misleading because of the strong bias caused by selecting systems with different stellar masses (Nigoche-Netro et al. 2008). Indeed, we found a clear trend when different intervals of absolute magnitude are considered in agreement with Nigoche-Netro et al. (2007, 2008), who pointed out how the KR coefficients and rms deviation from the fitted relation change when choosing fixed-width intervals of progressively brighter absolute magnitude.

Our bulges are consistent with the magnitude-dependent trend of the KR, and 5 of them lie in the poorly populated region of the low-mass systems characterized by small  $r_e$  and large  $\langle \mu_e \rangle$  (Fig. 5). The offset of the bulge of SDSSJ1152 is explained by the large errors on  $r_e$  and  $\langle \mu_e \rangle$ . Indeed, the data point is consistent within  $3\sigma$  with its magnitude bin. Owing to the large scatter and overall dependence on the mass of the KR, we cannot infer

any difference in the populations of bulges using such a relation, which is indeed a poor proxy to disentangle bulge properties.

### 5.3. Faber-Jackson relation

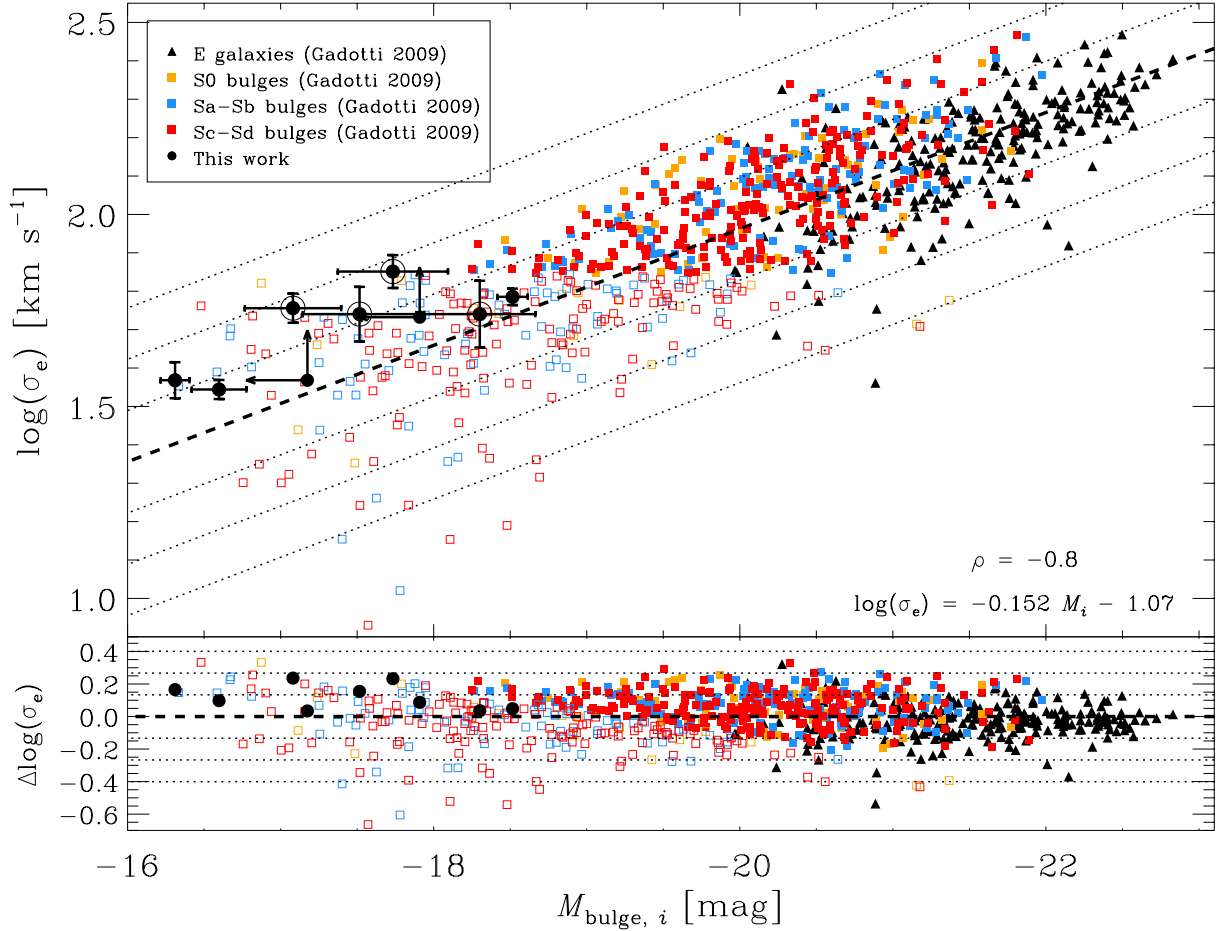
The FJR (Faber & Jackson 1976; Falcón-Barroso et al. 2011) states that brighter galaxies exhibit larger velocity dispersion.

Figure 6 shows the FJR for the comparison sample of ellipticals and bulges with the best-fitting line given by

$$\log(\sigma_e) = -0.152(\pm 0.003)M_i - 1.07(\pm 0.07), \quad (12)$$

where  $\sigma_e$  is provided in km s<sup>-1</sup> and  $M_i$  is the  $i$ -band absolute magnitude of the galaxy spheroid. We derived the FJR coefficients using the `poly_fit` routine in IDL. Equation (12) results in  $L \propto \sigma_e^{2.64 \pm 0.01}$ , which deviates from the theoretical virial relation  $L \propto \sigma_e^4$ , but it is consistent with  $L \propto \sigma_e^{2.9 \pm 0.5}$  found by Balcells et al. (2007) for a sample of bulges observed with the *Hubble* Space Telescope in the  $K$  band. The Pearson correlation coefficient is  $\rho = -0.8$ , reflecting a tight correlation between galaxies properties in this plane.

The scatter increases in the low- $\sigma$  end of the relation, showing a trend mimicking the expected down-bending of the FJR



**Fig. 6.** As in Fig. 4 but for the FJR and with the rms deviation in  $\log(\sigma_e)$  from the fit. The best-fitting relation and Pearson correlation coefficient are also given.

(Falcón-Barroso et al. 2011). This regime of the FJR is populated by the small bulges of the comparison sample. Their velocity dispersions are far below the instrumental resolution of the SDSS spectra. Moreover, they are measured within a fixed aperture of 3 arcsec, where a significant contamination from the disk component is expected because of the small  $B/T$  of these galaxies. On the contrary, no hint of down-bending is observed for our bulges, which have measured  $\sigma$  larger than instrumental resolution. At face values, they are above the FJR whereas disk-like bulges are expected to be low- $\sigma$  outliers, being rotation rather than pressure supported. As a matter of fact, each of our bulges follows the same FJR of the brighter ellipticals and bulges of the comparison sample. Moreover, we can infer that both ellipticals and bulges share the same properties when the FJR is used. The FJR down-bending highlighted in other works (Méndez-Abreu et al. 2008a; Kim et al. 2016) could be due to selection effects, when only high- or low-mass systems are considered. Indeed, the slope of the relation changes when galaxies with increasing values of absolute magnitudes are considered (Nigoche-Netro et al. 2010).

We did not observe any trend when bulges are divided according to the morphological type of their host galaxies (Fig. 6), in agreement with the results by Thomas & Davies (2006). They found that the stellar populations of less massive bulges are typically younger, less metal-rich, and less overabundant of  $\alpha$  elements than ETGs with no dependence on the morphological type. This also supports the correlation between the structural

parameters (e.g.,  $r_e/h$  and  $B/T$ ) and bulge luminosity and mass rather than morphological type.

We observed a smooth transition from larger to smaller values of  $n$  according to both  $\sigma$  and  $M_{\text{bulge},i}$  when the sample is divided in terms of the Sérsic index (Fig. 7). This suggests that  $n$  strongly depends on the mass of the system. The same trend is visible when  $B/T$  is considered (see Eq. (7) in Sect. 3.3). Recently, Kim et al. (2016) have shown that faint galaxies ( $-19 < M_{r,\text{bulge}} < -17$  mag) with smaller  $B/T$  have systematically lower  $\sigma$  than those with larger  $B/T$ . They concluded that bulges in low- $B/T$  galaxies are rotation supported (i.e., disk-like bulges). However, this is due to a bias caused by a priori selection of the  $B/T$  range used for fitting the FJR. Moreover, this selection leads to contradictory results because for brighter galaxies ( $M_r \lesssim -20$  mag) a smaller  $B/T$  corresponds to a larger  $\sigma$  (see their Fig. 9).

## 6. Discussion

The seven late-type bulges we studied in this work are small and have a low mass, as confirmed by their position in the FPR (Fig. 4), KR (Fig. 5), and FJR (Fig. 6). Although they are located at the low- $r_e$  and low- $\sigma$  ends of the scaling relations, they follow the same trend of ellipticals and larger and more massive bulges. To address the statistical significance of our claim, we computed the probability of each bulge to be compatible with the fitted relations by means of MC simulations. The deviation of each bulge from the FPR and FJR is less than 2.1 rms, therefore we can not

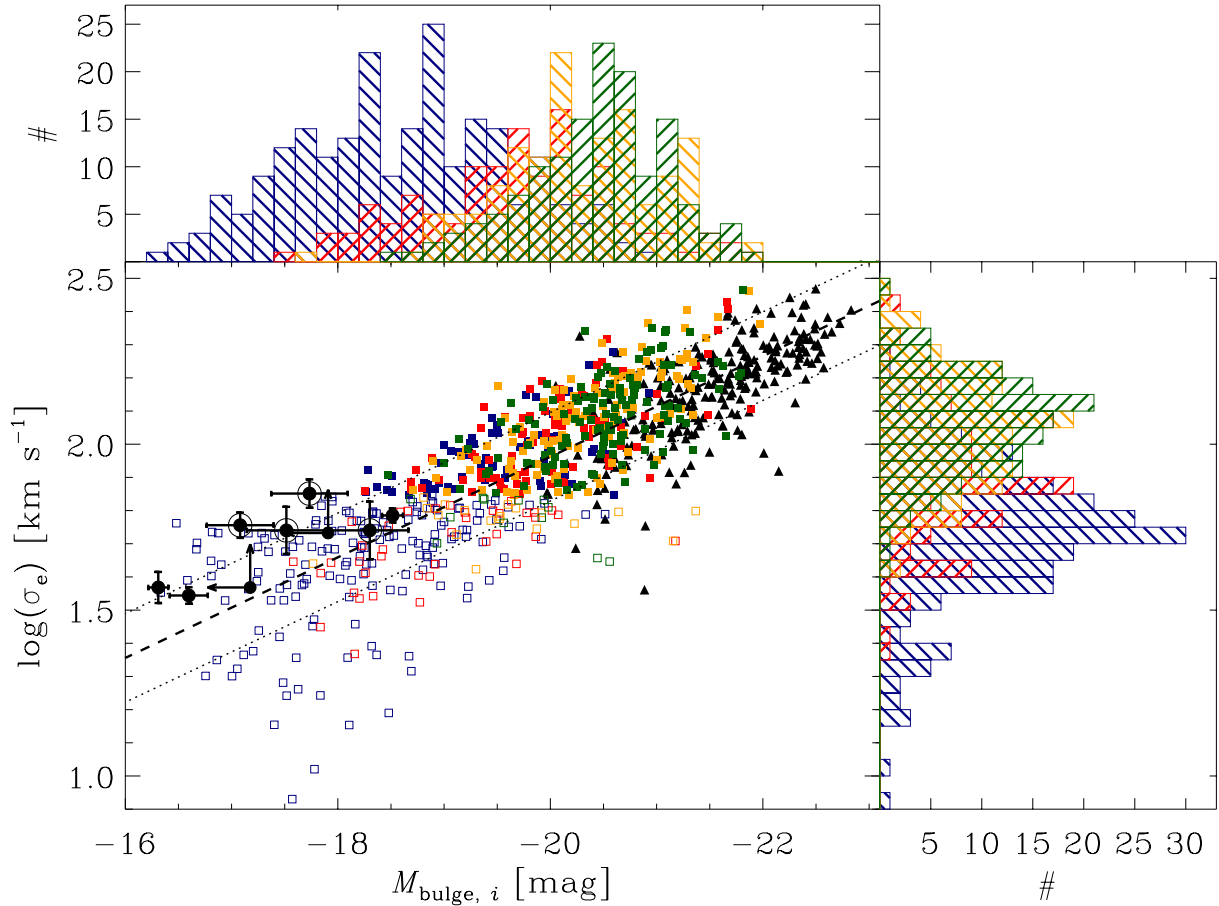


**Fig. 7.** Faber-Jackson relation for the galaxies of our (larger symbols) and comparison sample (smaller symbols). The ellipticals (triangles) and bulges (squares) of the comparison sample are shown with filled ( $\sigma > 70 \text{ km s}^{-1}$ ) and empty symbols ( $\sigma < 70 \text{ km s}^{-1}$ ) according to their calculated velocity dispersion. Filled circles with and without error bars correspond to the galaxies in our sample with and without bulge, respectively. Open circles indicate the barred galaxies. The galaxies are divided according to their Sérsic index in the following bins:  $1 < n < 2$  (blue),  $2 < n < 3$  (red),  $3 < n < 4$  (orange), and  $n > 4$  (green). The dashed line is the best-fitting relation for the comparison sample. The dotted lines show the rms deviation in  $\log(\sigma_e)$  given in Fig. 6. The distribution of galaxies of the different bins of  $n$  as function of their absolute magnitude and effective velocity dispersion are also shown.

consider them outliers. We found no differences between photometric and kinematic properties of barred and unbarred galaxies. The remaining two galaxies SDSSJ1040 and SDSSJ1121 were better fitted only with a disk component. This means that either they have no bulge or their bulge is really small and beyond our possibility to detect it. The latter reinforces the finding that small bulges are not low- $\sigma$  outliers in FJR.

As far as the structure and kinematics of disk-like bulges concerns, they are expected to share the properties of the surrounding host disks and be more rotation-dominated than classical bulges. Our seven bulges fulfill many of the observational prescriptions originally provided by Kormendy & Kennicutt (2004) and later revised by Kormendy (2016) as classified as disk-like bulges. They have a late-type morphology with a nearly exponential light profile, small  $B/T$ , low velocity dispersion, and ongoing star formation, as proved by the presence of strong  $H\beta$  and  $[O\text{III}]5007$  emission lines in their spectra. All the galaxies of our sample exhibit either a spiral structure all the way down to the galaxy center or a bar component (Fig. 2). In this case the bulge dynamics should be more similar to that of a disk rather than a spheroidal component, making the bulge a low- $\sigma$  outlier in the FJR. But our bulges are not rotation-dominated systems ( $v_{\text{max}} \leq 50 \text{ km s}^{-1}$ ), although they are characterized by very low values of velocity dispersion ( $\sigma_e \lesssim 70 \text{ km s}^{-1}$ ). Each of them

follows the same scaling relations of ellipticals, massive bulges, and compact early-type galaxies so they cannot be classified as disk-like systems.

We explored the possibility that our bulges could actually be similar to other spheroidal systems, such as globular clusters (GCs) and compact ETGs (cETGs). To this aim, we further extended the  $M_i$  and  $\sigma_e$  ranges of the FJR by including 125 GCs of the nearby giant elliptical NGC 5128 (Taylor et al. 2015) and 8 low-mass cETGs of the Virgo cluster (Guérou et al. 2015). We transformed the absolute magnitude of the GCs in the  $i$  band using the prescriptions from SDSS-DR8<sup>3</sup> (Aihara et al. 2011). Figure 8 shows that our bulges do not share the same position of GCs in the FJR even though they have similar values of velocity dispersion ( $\sigma_e \approx 30 \text{ km s}^{-1}$ ). The absolute magnitude of GCs is indeed several orders of magnitude fainter than that of small bulges. On the contrary, cETGs follow the same FJR as our bulges and more massive bulges. This supports the idea that the low SDSS-based values of velocity dispersion are in reality affected by instrumental resolution and disk contamination, and suggests that the less massive bulges follow the same scaling relations as ellipticals and more massive bulges.

<sup>3</sup> The equations are available in <https://www.sdss3.org/dr8/algorithms/sdssUBVRITransform.php#Lupton2005>

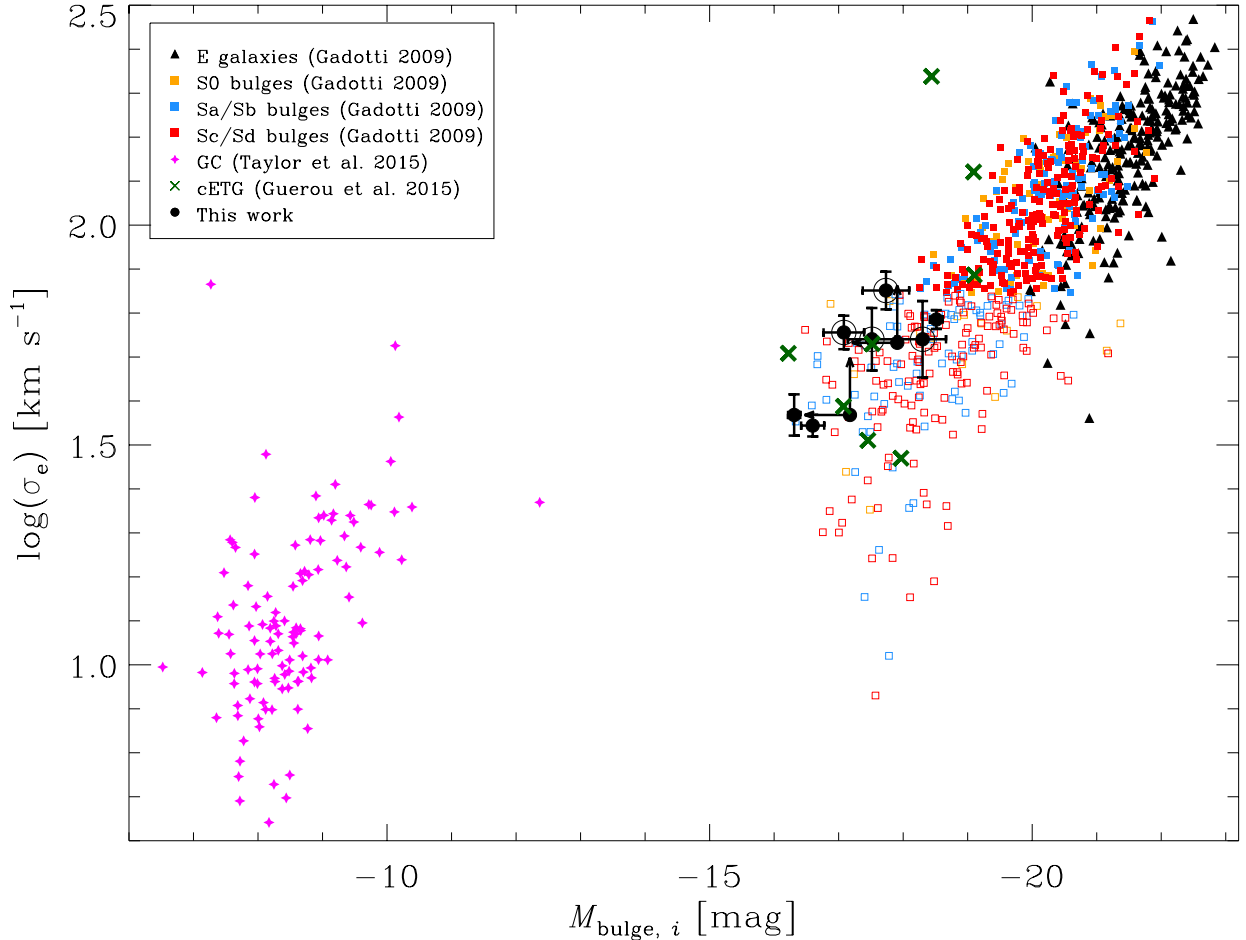


**Fig. 8.** As in Fig. 6 but including the GCs from Taylor et al. (2015, pink stars) and cETGs from Guérou et al. (2015, green crosses).

We found no correlation between the location of our bulges in the FPR or FJR and *Hubble* type of their host galaxies. The lack of correlation between the structural and kinematical properties of bulges and galaxy morphology is in agreement with the findings of Thomas & Davies (2006), who focused on the stellar population properties of bulges. The mass rather than the morphology seems to be the driver of the intrinsic physical properties of bulges. As a matter of fact, we found a single population of galaxy spheroids that follows the same scaling relations, where the mass leads to a smooth transition in the photometric and kinematical properties from less massive bulges to more massive bulges and ellipticals.

It is worth noticing that classical and disk-like bulge are usually separated only using the Sérsic index of their surface-brightness radial profile or even worse the Sérsic index of their host galaxy. This is a misuse of the findings of Fisher & Drory (2008, 2010), who pointed out a bimodal distribution of the Sérsic index of bulges. Once bulge-disk decomposition was performed on galaxies separated according to their visual morphology, they found that classical bulges have  $n > 2$  while disk-like bulges have  $n < 2$ . To date, no physical explanation has been found for this behavior. Moreover, since the Sérsic index correlates with  $B/T$  in classical bulges (Fisher & Drory 2008; Gadotti 2009), the common belief is that disk-like bulges have  $B/T < 0.35$ . However, the photometric and kinematical properties of our bulges in the framework of the scaling relations of ellipticals and bulges show that small values of  $n$  and  $B/T$  do not guarantee that a bulge is disk-like.

## 7. Conclusions

We analyzed the surface-brightness distribution and stellar kinematics of a sample of late-type spirals. They were selected to investigate the photometric and kinematic properties of small bulges in order to understand whether they follow the same scaling relations traced by ellipticals and large bulges and if they are disk-like or classical bulges.

We obtained the structural parameters of the sample galaxies by performing a two-dimensional photometric decomposition of their SDSS *i*-band images. The surface-brightness distribution of each galaxy was assumed to be the sum of the contribution of a Sérsic bulge and an exponential disk. We included a Ferrers bar in fitting the images of four sample galaxies. We found a bulge component in seven galaxies, while the remaining two resulted in pure disk galaxies. We measured the stellar velocity dispersion within the bulge effective radius from long-slit spectra taken with high spectral resolution. All the sample bulges have small  $r_e$ , nearly exponential light profiles, small  $B/T$ , low  $\sigma$ , and ongoing star formation.

We combined the photometric ( $r_e$ ,  $\langle\mu_e\rangle$ , and  $M_i$ ) and kinematical parameters ( $\sigma_e$ ) of the sample bulges to study their location in the FPR, KR, and FJR. To this aim, we built the scaling relations defined for a comparison sample of nearby ellipticals and bulges with structural parameters and velocity dispersions measured from SDSS *i*-band images and spectra by Gadotti (2009) and Oh et al. (2011), respectively. Our data extend the scaling relations to the regime of bulges with  $r_e \approx 0.2$  kpc,

$\sigma_e \simeq 35 \text{ km s}^{-1}$ , and  $M_i \simeq -16 \text{ mag}$ . The FPR coefficients are consistent with the findings of Bernardi et al. (2003b), which are based on a much larger sample of ETGs and characterized by a smaller scatter. The location of the ellipticals and bulges in the FPR suggests that there is a single population of galaxy spheroids sharing the same physical properties. This is also true when our small bulges are considered. No differences appear in the residuals when galaxies are divided according to their morphological type. The sample bulges are actually small in size and mass, resulting from their location in the KR. We confirmed that this relation is a poor proxy of the bulge properties and its large intrinsic scatter and magnitude bias (Nigoche-Netro et al. 2008, 2010), although it is commonly used to disentangle between classical and disk-like bulges (e.g., Vaghmare et al. 2013; Mishra et al. 2017). Our small bulges with resolved  $\sigma$  are not following the down-bending previously reported in the low- $\sigma$  end of the FJR, but trace the same trend as ellipticals and large bulges. This supports the idea that the lowest values of the SDSS-based  $\sigma$  are actually affected by instrumental resolution and disk contamination. We observed a smooth transition in FJR from larger to smaller values of  $n$  according to both  $\sigma_e$  and  $M_i$  when the comparison sample is divided in terms of the Sérsic index. This suggests that  $n$  strongly depends on the mass of the system rather than on the morphology of the host galaxy.

Our bulges fulfill most of the observational prescriptions (Kormendy & Kennicutt 2004; Kormendy 2016) for being disk-like bulges. But they are not rotation dominated and follow the same scaling relations of ellipticals and larger and more massive bulges, where the mass seems to lead to a smooth transition in the photometric and kinematic properties from less to more massive systems. We conclude that small values of  $n$  and  $B/T$  do not guarantee that a bulge is disk-like and not classical.

*Acknowledgements.* We would like to thank Mauro D’Onofrio for his comments on the FPR and the referee, Elmo Tempel, for his suggestions that helped us to improve the way we presented our results. This work is supported by Padua University through grants 60A02-5857/13, 60A02-5833/14, 60A02-4434/15, CPDA133894. E.M.C. and L.M. acknowledge financial support from Padua University grants BIRD164402/16 an CPS0204, respectively. J.M.A. acknowledges support from the European Research Council Starting Grant (SEDMorph; P.I. V. Wild). L.C. acknowledges the School of Physics and Astronomy of the University of St. Andrews for hospitality while this paper was in progress. This research also made use of the HyperLeda Database (<http://leda.univ-lyon1.fr/>) and NASA/IPAC Extragalactic Database (NED) which is operated by the Jet Propulsion Laboratory, California Institute of Technology, under contract with the National Aeronautics and Space Administration (<http://ned.ipac.caltech.edu/>) We acknowledge the use of SDSS data (<http://www.sdss.org>).

## References

- Adelman-McCarthy, J. K., Agüeros, M. A., Allam, S. S., et al. 2008, *ApJS*, **175**, 297
- Aguerri, J. A. L., Balcells, M., & Peletier, R. F. 2001, *A&A*, **367**, 428
- Aguerri, J. A. L., Iglesias-Paramo, J., Vilchez, J. M., & Muñoz-Tuñón, C. 2004, *AJ*, **127**, 1344
- Aguerri, J. A. L., Elias-Rosa, N., Corsini, E. M., & Muñoz-Tuñón, C. 2005, *A&A*, **434**, 109
- Ahn, C. P., Alexandroff, R., Allende Prieto, C., et al. 2012, *ApJS*, **203**, 21
- Aihara, H., Allende Prieto, C., An, D., et al. 2011, *ApJS*, **193**, 29
- Andredakis, Y. C. 1998, *MNRAS*, **295**, 725
- Athanassoula, E. 2005, *MNRAS*, **358**, 1477
- Athanassoula, E. 2013, in *Secular Evolution of Galaxies*, eds. J. Falcón-Barroso, & J. H. Knapen (Cambridge, UK: Cambridge University Press), 305
- Athanassoula, E., Morin, S., Wozniak, H., et al. 1990, *MNRAS*, **245**, 130
- Balcells, M., Graham, A. W., & Peletier, R. F. 2007, *ApJ*, **665**, 1104
- Bender, R., & Moellenhoff, C. 1987, *A&A*, **177**, 71
- Bender, R., Burstein, D., & Faber, S. M. 1992, *ApJ*, **399**, 462
- Bernardi, M., Sheth, R. K., Annis, J., et al. 2003a, *AJ*, **125**, 1817
- Bernardi, M., Sheth, R. K., Annis, J., et al. 2003b, *AJ*, **125**, 1866
- Böker, T., Laine, S., van der Marel, R. P., et al. 2002, *AJ*, **123**, 1389
- Böker, T., Stanek, R., & van der Marel, R. P. 2003, *AJ*, **125**, 1073
- Bournaud, F. 2016, *Galactic Bulges*, **418**, 355
- Bureau, M., & Athanassoula, E. 2005, *ApJ*, **626**, 159
- Buta, R. J., Sheth, K., Athanassoula, E., et al. 2015, *ApJS*, **217**, 32
- Caon, N., Capaccioli, M., & D’Onofrio, M. 1993, *MNRAS*, **265**, 1013
- Cappellari, M., & Emsellem, E. 2004, *PASP*, **116**, 138
- Cappellari, M., Scott, N., Alatalo, K., et al. 2013, *MNRAS*, **432**, 1709
- Carollo, C. M., Stiavelli, M., de Zeeuw, P. T., & Mack, J. 1997, *AJ*, **114**, 2366
- Chung, A., & Bureau, M. 2004, *AJ*, **127**, 3192
- Combes, F., & Sanders, R. H. 1981, *A&A*, **96**, 164
- Conselice, C. J. 2003, *ApJS*, **147**, 1
- Corsini, E. M., Méndez-Abreu, J., Pastorello, N., et al. 2012, *MNRAS*, **423**, L79
- Corsini, E. M., Wegner, G. A., Thomas, J., Saglia, R. P., & Bender, R. 2017, *MNRAS*, **466**, 974
- de Lorenzo-Cáceres, A., Vazdekis, A., Aguerri, J. A. L., Corsini, E. M., & Debattista, V. P. 2012, *MNRAS*, **420**, 1092
- de Lorenzo-Cáceres, A., Falcón-Barroso, J., & Vazdekis, A. 2013, *MNRAS*, **431**, 2397
- de Souza, R. E., Gadotti, D. A., & dos Anjos, S. 2004, *ApJS*, **153**, 411
- Dekel, A., Sari, R., & Ceverino, D. 2009, *ApJ*, **703**, 785
- Djorgovski, S., & Davis, M. 1987, *ApJ*, **313**, 59
- D’Onofrio, M., Fasano, G., Varela, J., et al. 2008, *ApJ*, **685**, 875
- Dressler, A., Lynden-Bell, D., Burstein, D., et al. 1987, *ApJ*, **313**, 42
- Eggen, O. J., Lynden-Bell, D., & Sandage, A. R. 1962, *ApJ*, **136**, 748
- Eliche-Moral, M. C., Balcells, M., Aguerri, J. A. L., & González-García, A. C. 2006, *A&A*, **457**, 91
- Eliche-Moral, M. C., González-García, A. C., Balcells, M., et al. 2011, *A&A*, **533**, A104
- Erwin, P. 2004, *A&A*, **415**, 941
- Erwin, P. 2015, *ApJ*, **799**, 226
- Erwin, P., & Debattista, V. P. 2013, *MNRAS*, **431**, 3060
- Erwin, P., Saglia, R. P., Fabricius, M., et al. 2015, *MNRAS*, **446**, 4039
- Eskridge, P. B., Frogel, J. A., Pogge, R. W., et al. 2000, *AJ*, **119**, 536
- Faber, S. M., & Jackson, R. E. 1976, *ApJ*, **204**, 668
- Falcón-Barroso, J., Peletier, R. F., & Balcells, M. 2002, *MNRAS*, **335**, 741
- Falcón-Barroso, J., van de Ven, G., Peletier, R. F., et al. 2011, *MNRAS*, **417**, 1787
- Falcón-Barroso, J., Lyubenova, M., van de Ven, G., et al. 2017, *A&A*, **597**, A48
- Ferrers, N. M. 1877, *Quart. J. Pure and Appl. Math.*, **14**, 1
- Fisher, D. B., & Drory, N. 2008, *AJ*, **136**, 773
- Fisher, D. B., & Drory, N. 2010, *ApJ*, **716**, 942
- Fisher, D. B., & Drory, N. 2016, *Galactic Bulges*, **418**, 41
- Freeman, K. C. 1970, *ApJ*, **160**, 811
- Gadotti, D. A. 2009, *MNRAS*, **393**, 1531
- Gerhard, O. E. 1993, *MNRAS*, **265**, 213
- Graham, A. W., & Guzmán, R. 2003, *AJ*, **125**, 2936
- Graham, A. W., Driver, S. P., Petrosian, V., et al. 2005, *AJ*, **130**, 1535
- Guérou, A., Emsellem, E., McDermid, R. M., et al. 2015, *ApJ*, **804**, 70
- Hamabe, M., & Kormendy, J. 1987, in *Structure and Dynamics of Elliptical Galaxies*, eds. P. T. de Zeeuw (Dordrecht: D. Reidel Publishing Co), IAU Symp., **127**, 379
- Hopkins, P. F., Cox, T. J., Younger, J. D., & Hernquist, L. 2009, *ApJ*, **691**, 1168
- Huertas-Company, M., Aguerri, J. A. L., Bernardi, M., Mei, S., & Sánchez Almeida, J. 2011, *A&A*, **525**, A157
- Hyde, J. B., & Bernardi, M. 2009, *MNRAS*, **394**, 1978
- Jedrzejewski, R. I. 1987, *MNRAS*, **226**, 747
- Jorgensen, I., Franx, M., & Kjaergaard, P. 1996, *MNRAS*, **280**, 167
- Kauffmann, G. 1996, *MNRAS*, **281**, 487
- Kautsch, S. J., Grebel, E. K., Barazza, F. D., & Gallagher, III, J. S. 2006, *A&A*, **445**, 765
- Kim, K., Oh, S., Jeong, H., et al. 2016, *ApJS*, **225**, 6
- Kormendy, J. 1985, *ApJ*, **295**, 73
- Kormendy, J. 2016, *Galactic Bulges*, **418**, 431
- Kormendy, J., & Barentine, J. C. 2010, *ApJ*, **715**, L176
- Kormendy, J., & Kennicutt, Jr., R. C. 2004, *ARA&A*, **42**, 603
- Kormendy, J., Drory, N., Bender, R., & Cornell, M. E. 2010, *ApJ*, **723**, 54
- La Barbera, F., Busarello, G., Merluzzi, P., Massarotti, M., & Capaccioli, M. 2003, *ApJ*, **595**, 127
- La Barbera, F., de Carvalho, R. R., de La Rosa, I. G., & Lopes, P. A. A. 2010, *MNRAS*, **408**, 1335
- Laurikainen, E., & Salo, H. 2016, *Galactic Bulges*, **418**, 77
- Laurikainen, E., Salo, H., Buta, R., Knapen, J. H., & Comerón, S. 2010, *MNRAS*, **405**, 1089
- Lütticke, R., Dettmar, R.-J., & Pohlen, M. 2000a, *A&AS*, **145**, 405
- Lütticke, R., Dettmar, R.-J., & Pohlen, M. 2000b, *A&A*, **362**, 435

- Makarov, D., Prugniel, P., Terekhova, N., Courtois, H., & Vauglin, I. 2014, *A&A*, **570**, A13
- Markwardt, C. B. 2009, in *Astronomical Data Analysis Software and Systems XVIII*, eds. D. A. Bohlender, D. Durand, & P. Dowler, ASP Conf. Ser., 411, 251
- Méndez-Abreu, J., Aguerri, J. A. L., Corsini, E. M., & Simonneau, E. 2008a, *A&A*, **478**, 353
- Méndez-Abreu, J., Corsini, E. M., Debattista, V. P., et al. 2008b, *ApJ*, **679**, L73
- Méndez-Abreu, J., Simonneau, E., Aguerri, J. A. L., & Corsini, E. M. 2010, *A&A*, **521**, A71
- Méndez-Abreu, J., Debattista, V. P., Corsini, E. M., & Aguerri, J. A. L. 2014, *A&A*, **572**, A25
- Méndez-Abreu, J., Aguerri, J. A. L., Falcón-Barroso, J., et al. 2017a, *A&A*, submitted
- Méndez-Abreu, J., Ruiz-Lara, T., Sánchez-Menguiano, L., et al. 2017b, *A&A*, **598**, A32
- Mishra, P. K., Wadadekar, Y., & Barway, S. 2017, *MNRAS*, in press [[arXiv:1701.07641](https://arxiv.org/abs/1701.07641)]
- Moffat, A. F. J. 1969, *A&A*, **3**, 455
- Moré, J. J., Garbow, B. S., & E., H. K. 1980, Argonne National Laboratory Report ANL-80-74
- Morelli, L., Cesetti, M., Corsini, E. M., et al. 2010, *A&A*, **518**, A32
- Morelli, L., Parmiggiani, M., Corsini, E. M., et al. 2016, *MNRAS*, **463**, 4396
- Nair, P. B., & Abraham, R. G. 2010, *ApJS*, **186**, 427
- Nigoche-Netro, A., Moles, M., Ruelas-Mayorga, A., Franco-Balderas, A., & Kjergaard, P. 2007, *A&A*, **472**, 773
- Nigoche-Netro, A., Ruelas-Mayorga, A., & Franco-Balderas, A. 2008, *A&A*, **491**, 731
- Nigoche-Netro, A., Aguerri, J. A. L., Lagos, P., et al. 2010, *A&A*, **516**, A96
- Noguchi, M. 1999, *ApJ*, **514**, 77
- Oh, K., Sarzi, M., Schawinski, K., & Yi, S. K. 2011, *ApJS*, **195**, 13
- Peng, C. Y., Ho, L. C., Impey, C. D., & Rix, H.-W. 2002, *AJ*, **124**, 266
- Pohlen, M., & Trujillo, I. 2006, *A&A*, **454**, 759
- Press, W. H., Teukolsky, S. A., Vetterling, W. T., & Flannery, B. P. 1992, *Numerical recipes in FORTRAN. The art of scientific computing* (Cambridge, UK: Cambridge University Press)
- Prieto, M., Aguerri, J. A. L., Varela, A. M., & Muñoz-Tuñón, C. 2001, *A&A*, **367**, 405
- Prugniel, P., & Soubiran, C. 2001, *A&A*, **369**, 1048
- Ravikumar, C. D., Barway, S., Kembhavi, A., Mobasher, B., & Kuriakose, V. C. 2006, *A&A*, **446**, 827
- Sánchez, S. F., García-Benito, R., Zibetti, S., et al. 2016, *A&A*, **594**, A36
- Sarzi, M., Falcón-Barroso, J., Davies, R. L., et al. 2006, *MNRAS*, **366**, 1151
- Sérsic, J. L. 1968, *Atlas de Galaxias Australes* (Cordoba: Observatorio Astronomico de Cordoba)
- Seth, A. C., Dalcanton, J. J., Hodge, P. W., & Debattista, V. P. 2006, *AJ*, **132**, 2539
- Simard, L. 1998, in *Astronomical Data Analysis Software and Systems VII*, eds. R. Albrecht, R. N. Hook, & H. A. Bushouse, ASP Conf. Ser., 145, 108
- Taylor, M. A., Puzia, T. H., Gomez, M., & Woodley, K. A. 2015, *ApJ*, **805**, 65
- Tempel, E., Saar, E., Liivamägi, L. J., et al. 2011, *A&A*, **529**, A53
- Thomas, D., & Davies, R. L. 2006, *MNRAS*, **366**, 510
- Trujillo, I., Aguerri, J. A. L., Cepa, J., & Gutiérrez, C. M. 2001, *MNRAS*, **328**, 977
- Vaghmare, K., Barway, S., & Kembhavi, A. 2013, *ApJ*, **767**, L33
- van der Marel, R. P., & Franx, M. 1993, *ApJ*, **407**, 525
- Weinzirl, T., Jogee, S., Khochfar, S., Burkert, A., & Kormendy, J. 2009, *ApJ*, **696**, 411
- Zavala, J., Avila-Reese, V., Firmani, C., & Boylan-Kolchin, M. 2012, *MNRAS*, **427**, 1503

## Appendix A: Spatial resolution of the bulge component

We performed a further analysis to ensure that our bulges are spatially resolved because the angular sizes of most of them are close to the size of the image PSF ( $1.3 < r_e/\sigma_{\text{PSF}} < 6.9$ ), resulting from the photometric decomposition (Table 3).

To this aim, we built a large number of images of mock galaxies with a Sérsic bulge and an exponential disk belonging to the faintest magnitude bin ( $m_i = 15$  mag); the galaxies have a Moffat PSF with  $FWHM_{\text{PSF}} = 1$  arcsec consistent with observations and are characterized by different values of  $r_e$  so that  $r_e/\sigma_{\text{PSF}} = [1.2, 1.8, 2.4, 3.0, 3.5, 4.1, 4.7, 5.3, 5.9, 6.5, 7.1]$ . We chose the value of the Sérsic index to be  $n = [0.5, 1, 1.5, 2, 2.5, 3, 3.5, 4, 4.5, 5]$ . We generated the remaining structural parameters of the mock galaxies in two different ways. First, we adopted  $B/T = 0.1$  and derived  $h$  using the  $(r_e/h, B/T)$  correlation given in Eq. (8) to inspect galaxies with different disk sizes. Then, we adopted  $h = 5.6$  arcsec that is consistent with the disk scale lengths of our sample galaxies (Table 3) and randomly derived  $B/T$  from a uniform distribution in the range  $[0, 0.45]$  to examine the impact of the bulge component. We investigated all the possible permutations and built two final samples of 110 mock galaxies each, where all the geometrical parameters are the same for all the galaxies in the same sample. We analyzed the images of the mock galaxies as if they were real using GASP2D.

The two different sets of mock galaxies lead to the same results (Figs. A.1 and A.2). The bulge component can be actually measured even if  $r_e/\sigma_{\text{PSF}} = 1.2$  with a relative error  $\sigma_{r_e, \text{syst}}/r_e \lesssim 0.1$  in agreement with the photometric errors from the MC analysis. If brighter galaxies are considered (e.g., with  $m_i = 13$  mag) the errors on  $r_e$  become smaller ( $\sigma_{r_e, \text{syst}}/r_e \sim 0.01$ ). Therefore, all the sample bulges are spatially resolved. We also considered the role of  $n$  (Fig. A.1) and  $\mu_e$  (Fig. A.2). Galaxies with smaller  $n$  are better fitted than those with larger  $n$ . Moreover, galaxies with larger  $\mu_e$  show a larger scatter around the actual value. This combined effect could be explained by the fact that smaller bulges are also brighter and so their parameters are retrieved with greater accuracy.

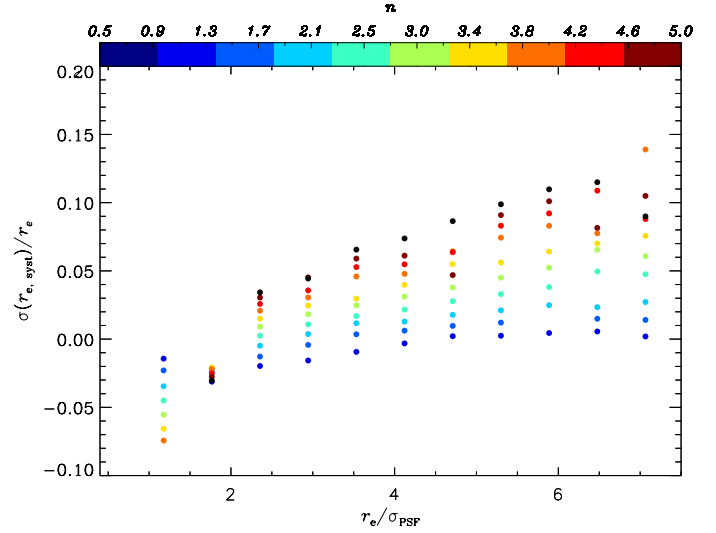


**Fig. A.1.** Relative difference between  $r_{e, \text{output}}$  and  $r_{e, \text{input}}$  as function of  $r_e/\sigma_{\text{PSF}}$  adopting  $B/T = 0.1$ . Positive/negative values correspond to an over/underestimation of  $r_e$ . The different values of  $n$  are shown in different colors.

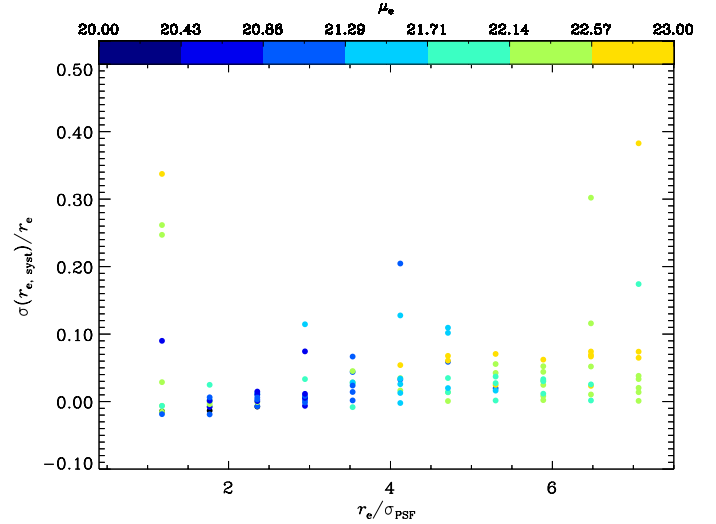


**Fig. A.2.** Relative difference between  $r_{e, \text{output}}$  and  $r_{e, \text{input}}$  as function of  $r_e/\sigma_{\text{PSF}}$  adopting  $h = 5.6$  arcsec. Positive/negative values correspond to an over/underestimation of  $r_e$ . The different values of  $\mu_e$  are shown in different colors.

Appendix B: Additional tables

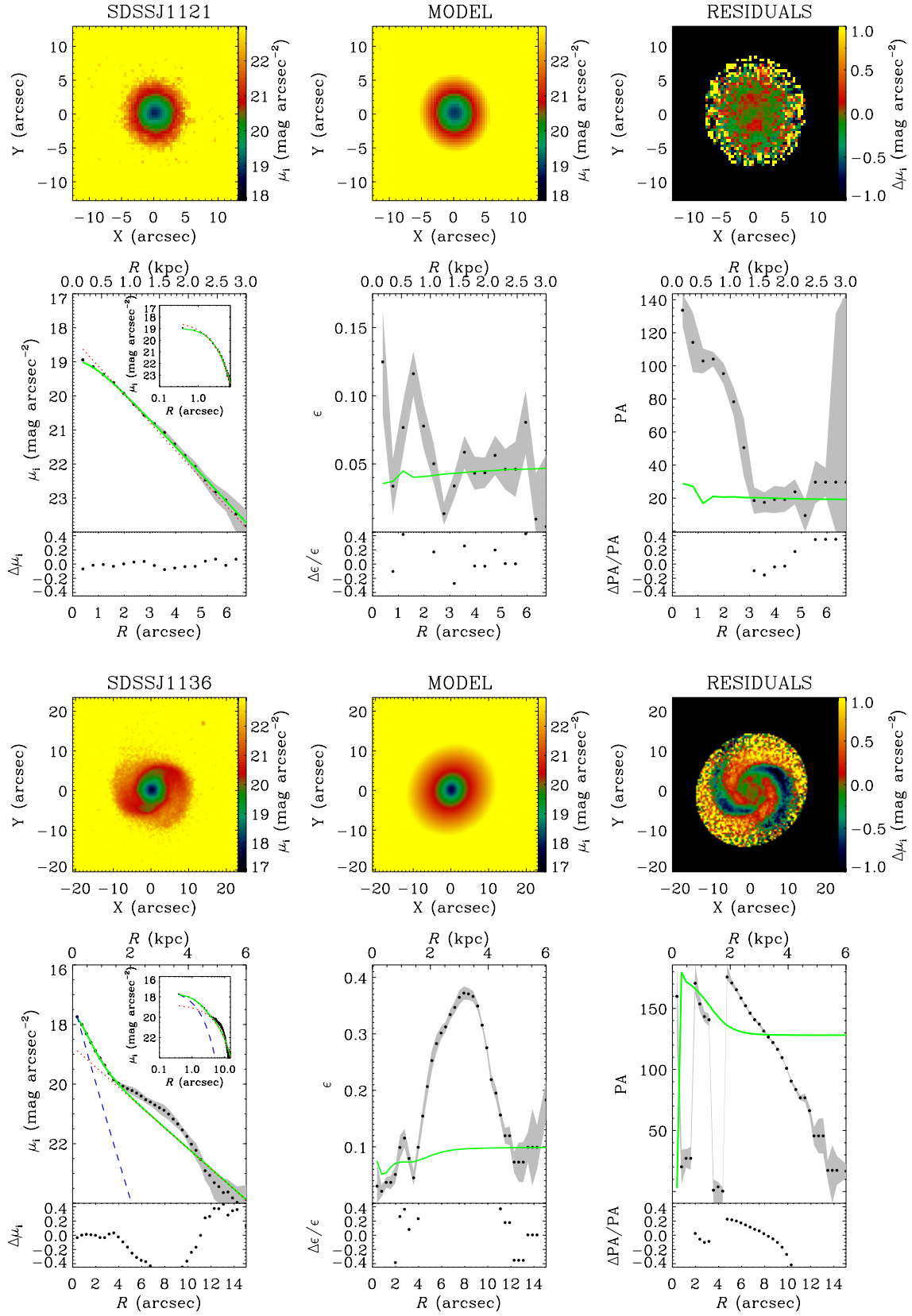


Fig. B.1. Complete version of Fig. 2. For details see caption of Fig. 2.

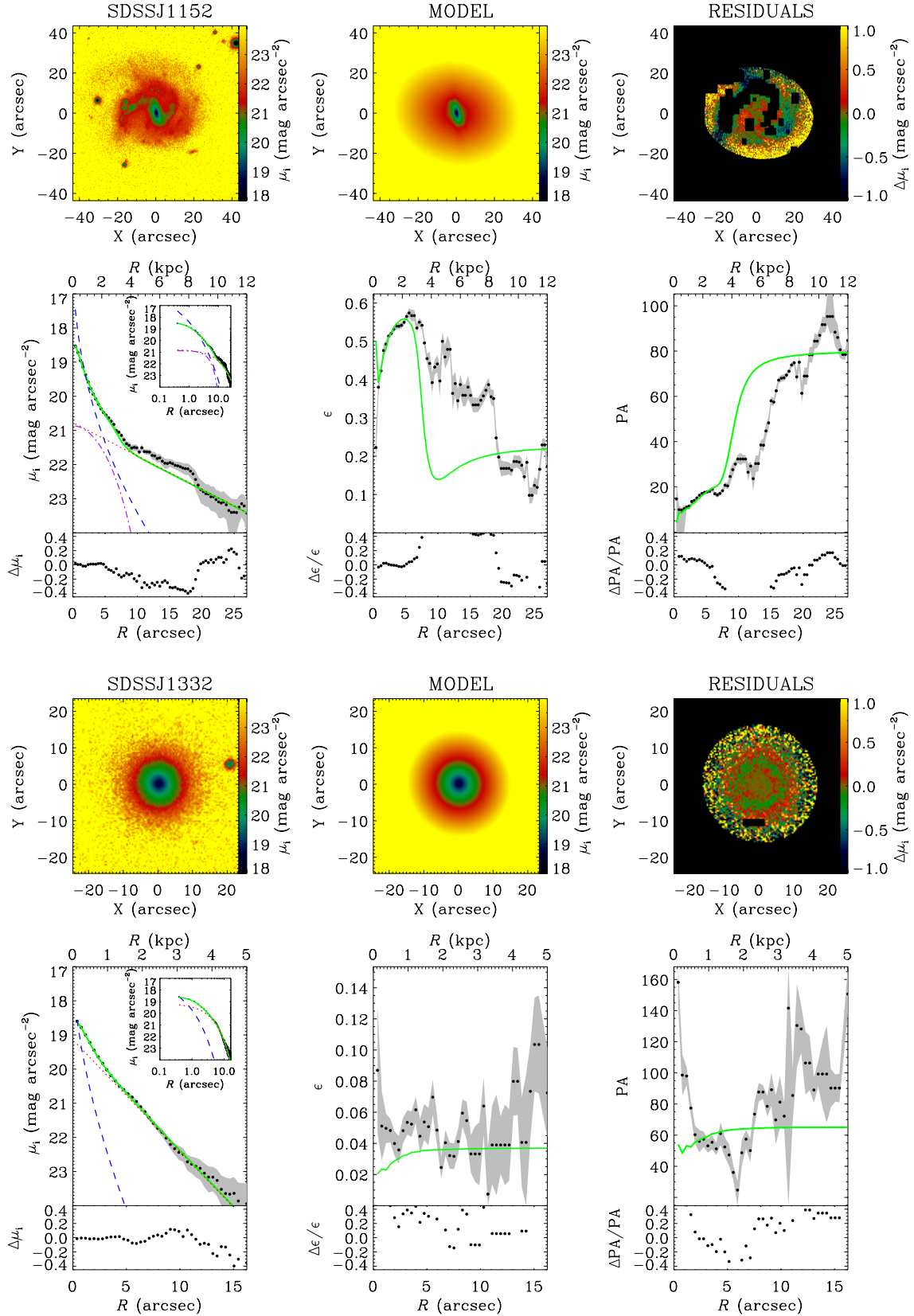


Fig. B.1. continued.

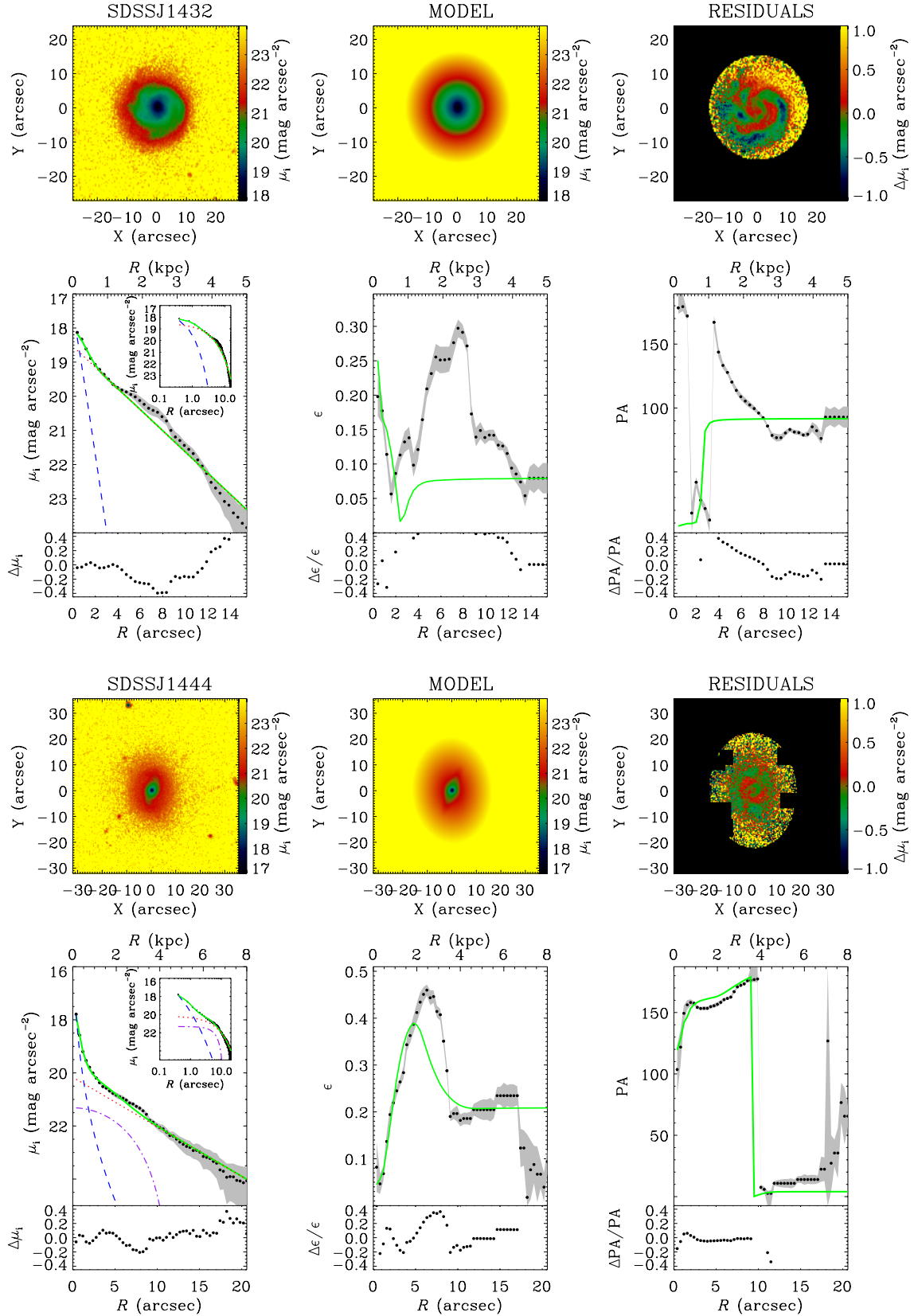


Fig. B.1. continued.

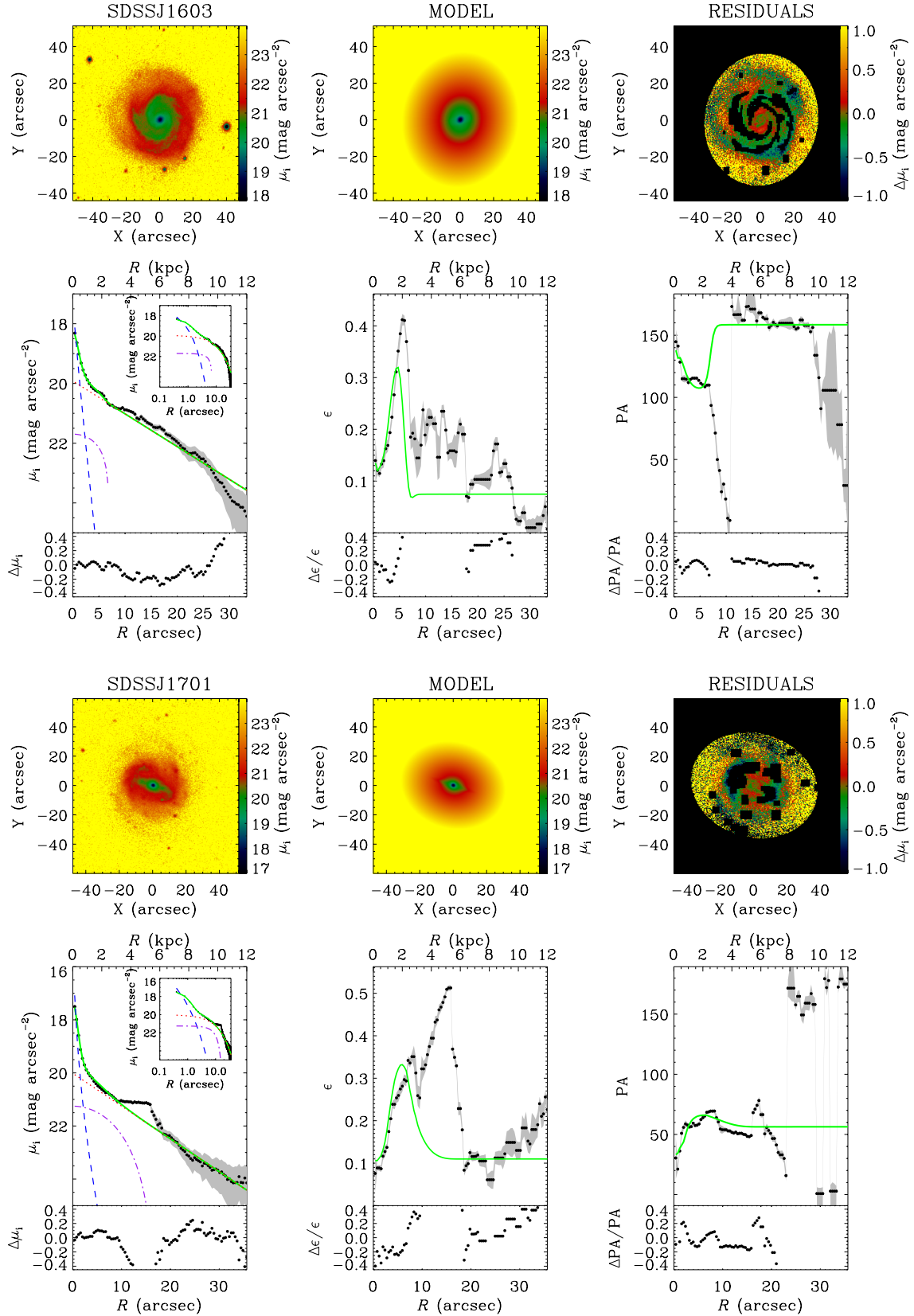


Fig. B.1. continued.